Spring 5-2019

Modeling and Characterization of a Ring-Resonator based Silicon Photonic Sensor on Silicon-on-Insulator (SOI)

Gwangho Choi
Rose-Hulman Institute of Technology, choig@rose-hulman.edu

Modeling and Characterization of a Ring-Resonator based Silicon Photonic Sensor on Silicon-on-Insulator (SOI)

A Thesis

Submitted to the Faculty

of

Rose-Hulman Institute of Technology

by

Gwangho Choi

In Partial Fulfillment of the Requirements for the Degree

of

Master of Science in Optical Engineering

May 2019

ROSE-HULMAN INSTITUTE OF TECHNOLOGY

Final Examination Report

Gwang Ho Choi — Name

Optical Engineering — Graduate Major

Thesis Title: Modeling and Characterization of a Ring-Resonator based Silicon Photonic Sensor on SOI

DATE OF EXAM: February 1, 2019

EXAMINATION COMMITTEE:

	Thesis Advisory Committee	Department
Thesis Advisor:	Azad Siamakoun	PHOE
	Sergio Granieri	PHOE
	Won-Jong Joo	SNUST

PASSED X **FAILED** _____

ABSTRACT

Choi, Gwangho

M.S.O. E.

Rose-Hulman Institute of Technology

May 2019

Modeling and Characterization of a Ring-Resonator based Silicon Photonic Sensor on Silicon-on-Insulator (SOI)

Thesis Advisor: Dr. Azad Siahmakoun

The purpose of this work is to build silicon photonic devices and verify their functionalities. In particular, the structure of a ring resonator (RR) is analyzed and applied to various silicon photonic application in sensing. Silicon waveguides, grating couplers, directional couplers, and RRs are fabricated on the silicon-on-insulator (SOI) wafer. Geometrical parameters and optical properties of the silicon devices are studied and also applied to the design of the aforementioned devices. The waveguide dimensions and, optical properties of the silicon waveguide such as dispersion and effective-index are examined. The RRs are made of a series of straight and bent waveguides which are analyzed as a function of their geometrical variables such as path length of ring resonator and the gap between the bus and the bent waveguide forming the RR. Device fabrication is done in collaboration with the University of Minnesota where the Electron-beam lithography is performed. Finally, the devices are tested, and their performance is characterized. The average measured channel spacing between four channels of an integrated wavelength-division multiplexer is 1.825 ± 0.01 nm. The experimental errors and their corresponding factors are discussed in details since

the measured data reveal the devices performed inefficiently when compared to the simulations and theoretical predictions.

ACKNOWLEDGEMENTS

I would like to express my sincere appreciation to my advisor, Professor Azad Siahmakoun, for your support and encouragement. You guided me in the right direction with patience whenever I lost my way in my research and was unsure of what to do. I will never forget your efforts and time that you provided for me.

I would also like to appreciate Professor Wonjong Joo, my advisor in SeoulTech. You have always believed in me and encouraged me to be a better person. You are a mentor not only in the path of research but also in the path of life.

I would additionally like to thank my committee member, Dr. Sergio C. Granieri, for agreeing to serve as a member without hesitation.

TABLE OF CONENTS

LIST OF FIGURES

Figure **Page**

LIST OF TABLES

Table **Page**

LIST OF ABBREVIATIONS

SOI	Silicon-on-Insulator
SEM	Scanning Electron Microscopy
TE	Transverse Electric
TM	Transverse Magnetic
WDM	Wavelength Division Multiplexer
FSR	Free Spectral Range
FWHM	Full-width half-maximum
FDTD	Finite-Difference Time-Domain
varFDTD	Variational FDTD
LCML	Lumerical Compact Model Library
BOE	Buffered oxide etch
PDK	Package Design Kit
FOV	Field of view
PM	Polarization maintaining
OSA	Optical Spectrum Analyzer
PICs	Photonic Integrated Circuits
I/O	Input / Output

LIST OF SYMBOLS

English symbols

n_g	Group index
α	Field attenuation coefficient
a_2	Amplitude of light before coupling to a ring cavity
b_2	Amplitude after coupling to a ring cavity
a_1	Normalized amplitude of input wave
T	Transmission spectrum
ΔP	Variations of circumference of a ring resonator
a	Total absorption coefficient
a_I	Intrinsic waveguide loss
a_A	Absorption by an analyte

Greek Symbols

$\boldsymbol{\theta_i}$	Incident angle
$\boldsymbol{\theta}$	Phase change over one round trip in a ring resonator
$\boldsymbol{\phi_t}$	Phase change due to coupling section
$\boldsymbol{\Gamma}$	Confinement factor

1. INTRODUCTION

For decades, optical sensors have been subject of intense research as we continue to develop methods to integrate photonic devices into a chip and other silicon photonic technologies. Optofluidic techniques are becoming a popular method due to their potential in biochemical applications and miniaturization into silicon chips. However, as devices are integrated into a chip, their sensing efficiency is also reduced due to a decrease in the interaction region of light with the materials. Researchers have demonstrated cavity-enhanced methods to maximize interaction lengths using cavity structures such as ring resonators [1]–[4]. Absorbance-based sensing techniques are attractive because of their ability to obtain label-free spectral information, while refractive index sensors can be easily affected by other factors such as non-target molecules or thermal fluctuations [3], [5]–[10].

In this thesis, we report on ring-resonator based fluidic-sensors of various dimensions and compare the experimental results with the theoretical estimations. This passive device is also further studied with an integration of wavelength-division multiplexer to demonstrate passive detection scheme. By comparison, the previous work by others require tuning or sweeping of the laser source wavelength in order to obtain the spectral information.

2. THEORY

In this section, we discuss the basic characteristics of strip waveguides such as geometries, effective index, group index, loss, and polarization modes of the light. There are two kinds of polarization modes; transverse-electric (TE) mode and transverse-magnetic (TM) mode, which are formed based on their field orientation. Basic calculations and their simulations are presented. The ring resonators based on silicon strip waveguides will be characterized by their design parameters. The parameters are essential factors evaluating the performance of ring resonators. Basic configurations of ring resonators (RRs) are given. The ring resonator-based sensors and the wavelength division multiplexer (WDM) are discussed. The first case consists of one straight bus waveguide and a ring resonator, while the second case is comprised of two-bus waveguide and a ring resonator. Finally, methods for obtaining an absorption spectra of the sensor is described.

2.1. The Silicon Waveguide

A waveguide is an essential structure to deliver light throughout the silicon photonic circuit which consists of waveguides and combinations. To select a proper geometry, material and methods of fabrication cannot be ignored in order to build effective silicon photonic devices. Silicon-on-insulator (SOI) is chosen in that it has a high refractive-index contrast between the core (silicon), and cladding (air and silicon dioxide). This high refractive-index contrast allows the light to be well-confined in the waveguide. The structure of a strip waveguide is shown in Figure 2.1. The waveguide is 500 nm wide and 220 nm thick (1 μm length is considered in a simulation manner). However, note that the simulation only takes into account the cross section of the waveguide.

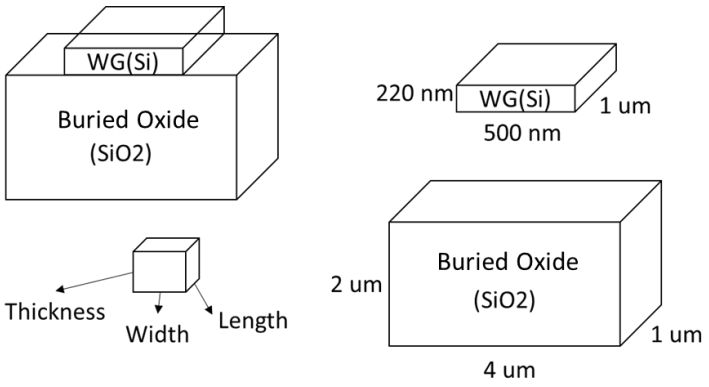

Figure 2.1 Typical structure of an SOI strip waveguide

The oxide layer is expected to be more than 1 μm thick in order to minimize leakage allowing the light to decay over the layer exponentially. The number of modes propagating through the waveguide depends on the structure of the waveguide. If the waveguide width is too wide, multiple modes are able to propagate, which will introduce loss. We adopted the reported data to design waveguides and verified with the Lumerical Software [4] as shown in Figure 2.2.

Since the refractive indices of the silicon and silicon dioxide are dispersive, i.e. depend on the wavelength, and the height and width of the waveguide are factors of the optical confinement, the effective index will also be dependent on the wavelength and dimensions of the waveguide. The total dispersion ($dn_{eff}/d\lambda$) of a guided mode can be expressed by the sum of material dispersion and waveguide dispersion. The material dispersion is dependent on the material and the waveguide dispersion relies on a guided mode. The group index (Equation (2.1)) can be used to determine the free-spectral range (FSR) of the ring resonator filter.

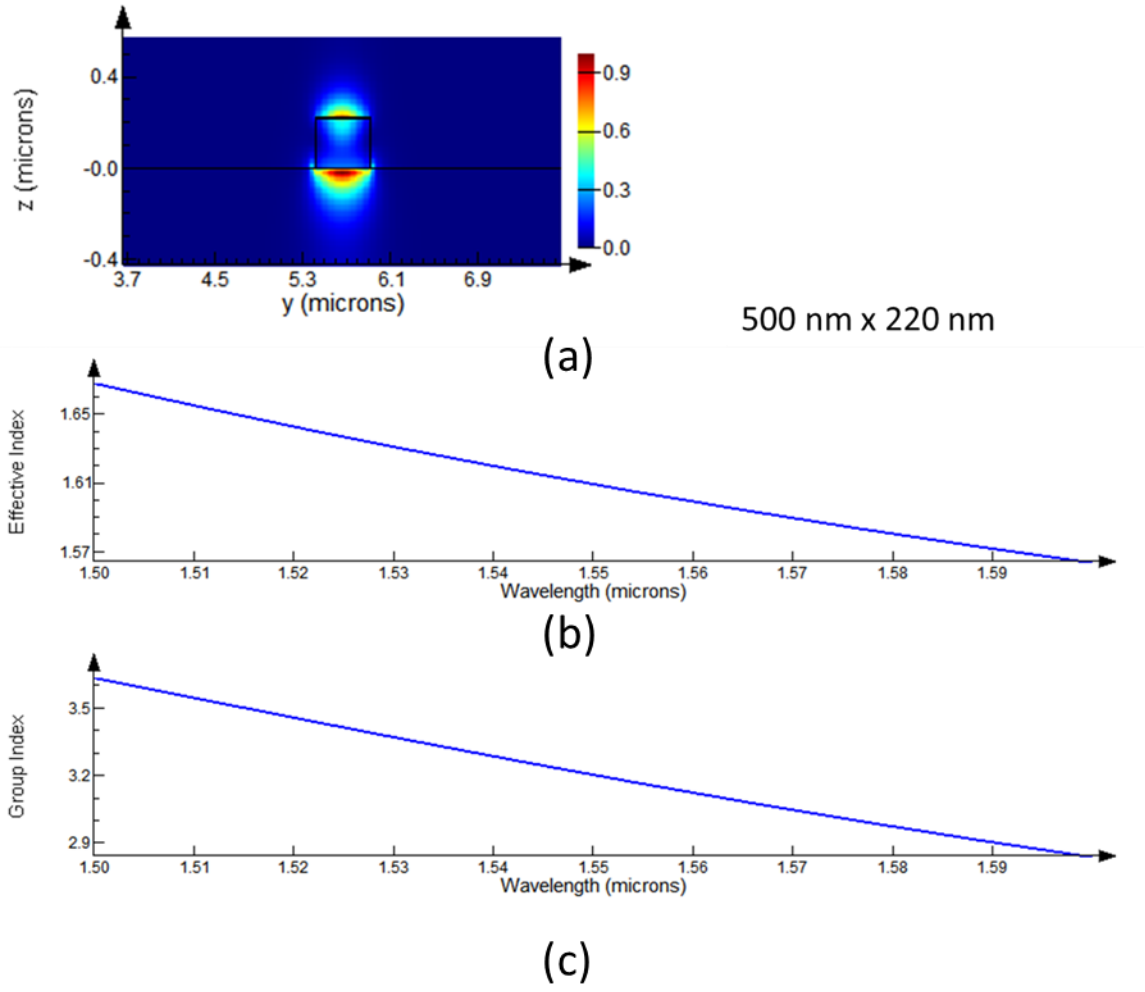

Figure 2.2 (a) TM mode propagation simulation for 500x200 nm geometry, (c) effective index and (c) group index figures as a function of the wavelength are presented.

$$n_g = n_{eff} - \lambda \frac{dn_{eff}}{d\lambda} \tag{2.1}$$

where n_{eff} is the effective index. When the waveguide width is fixed to 500 nm and height to 220 nm, we use a Lumerical simulation software to obtain effective indices and group indices as shown in Figure 2.2. The effective index decreases as the wavelength increases, which means

less confinement of the optical mode resulting from its dispersive refractive index properties. Figure 2.2 presents two possible optical modes, where their effective indices are greater than the refractive index of the silicon dioxide (typically 1.45). For the purpose of the optical sensor, The TM mode is selected to yield a better interaction between the light and the chemical solution. The TM mode shows a smaller effective index and less confinement than the TE mode, as shown in Figure 2.3 and Figure 2.4. Details of calculated values are shown in Table 2.1.

When the energy confinement is the only deciding factor of the mode, the fundamental TE mode should be chosen to deliver light more efficiently. However, at the cost of the leakage of optical power, the TM mode is selected to allow more power of the light to be in contact with the analyte, which results in a longer effective interaction length and thus leading to increase sensitivity.

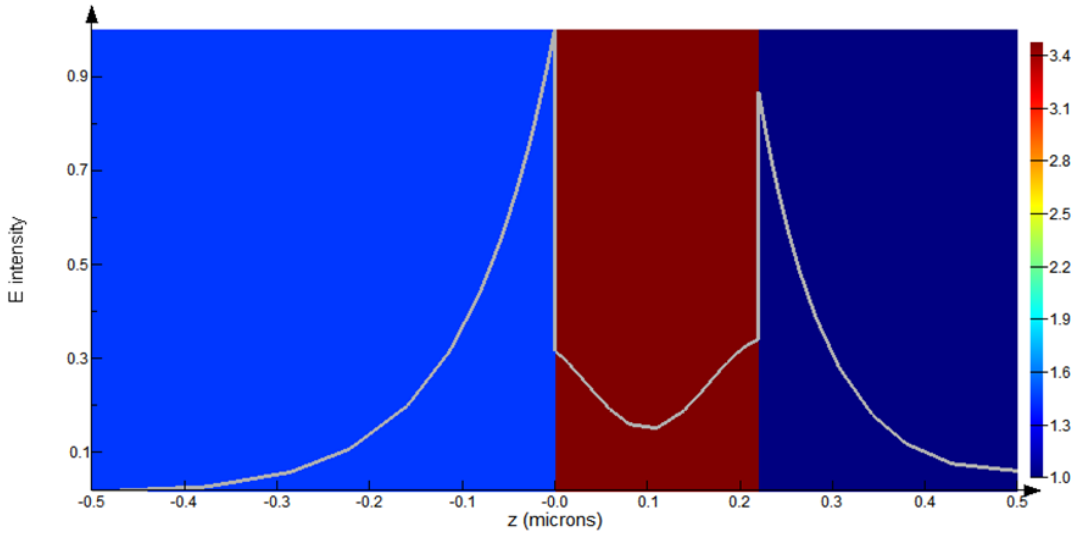

Figure 2.3 TM mode intensity profile over the vertical direction. The TM mode (mode #2) has smaller effective indices than the TE mode (mode #1).

Table 2.1 Effective index for TE and TM mode. TE polarization fraction indicates whether the mode is TE or TM mode.

Mode #	Effective index	Wavelength	TE polarization fraction
TM mode propagation (2D)			
1	2.445320	1.5	98
2	1.668016	1.5	6
TM mode propagation (3D)			
1	2.826793	1.54839	100
2	1.920616	1.54839	0
TM mode propagation (with loss)			
1	2.882428	1.5	100
2	1.675070	1.5	0

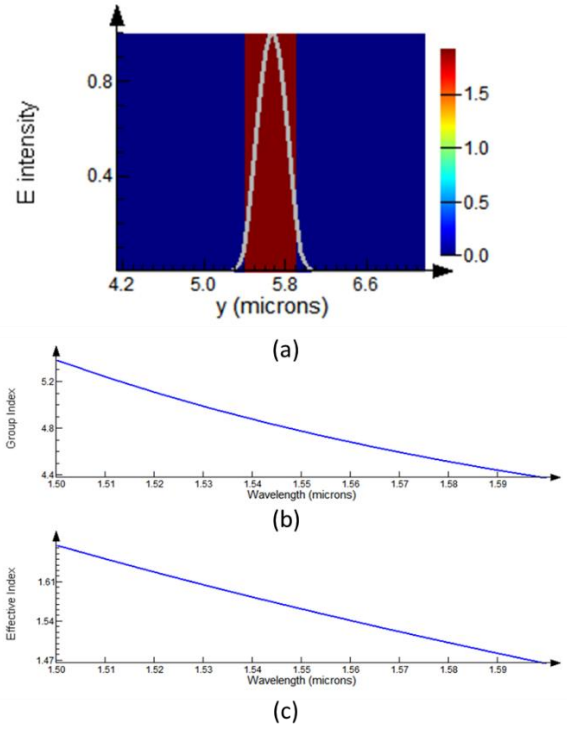

Figure 2.4 (a) Fundamental TE-mode profile is simulated, and (b) group index and (c) effective index graphs in the given geometry are given.

2.2. Ring Resonators

A simplified configuration of a ring resonator is presented in Figure 2.5. As light arrives at the coupling region, some amount of light couples into the ring cavity while the rest of the light goes through the bus waveguide. When the coupling is lossless and a single polarization is considered, one can describe a matrix relationship between the input and output amplitudes of the light [11].

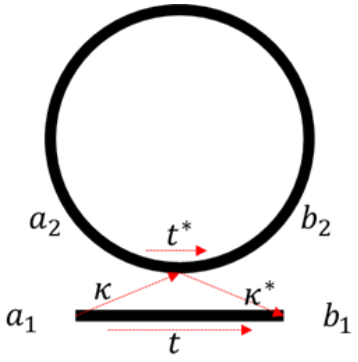

Figure 2.5. Basic ring resonator configuration. When the input light (a_1) is injected, some fraction of the light (κ) is evanescently coupled into the ring resonator, κ is the coupling coefficient and t is the transmission coefficient.

$$\begin{pmatrix} b_1 \\ b_2 \end{pmatrix} = \begin{pmatrix} t & \kappa \\ -\kappa^* & t^* \end{pmatrix} \begin{pmatrix} a_1 \\ a_2 \end{pmatrix} \tag{2.2}$$

where the complex mode amplitudes b_i, a_i $(i = 1, 2)$ are normalized values. As we assumed the ring resonator is lossless at the coupling region, the following expression is valid [12], [13].

$$|\kappa|^2 + |t|^2 = 1 \tag{2.3}$$

where κ is the coupling coefficient and t is the transmission coefficient. As the light travels around the ring, it experiences phase delay and amplitude attenuation. One can express this relation using the equation below:

$$a_2 = \alpha e^{j\theta} b_2 \tag{2.4a}$$

where the phase change over one round trip of the ring resonator is given by:

$$\theta = \beta L = k \cdot n_{eff} \cdot L = (2\pi \cdot n_{eff} \cdot L)/\lambda \tag{2.4b}$$

where α is the field attenuation coefficient, a_2 is the amplitude of the light before coupling from the ring cavity, and b_2 is the amplitude after coupling at the ring cavity.

When the normalized amplitude of the input wave ($a_1 = 1$) is considered, the complex field amplitude value passing the coupling section of the bus waveguide can be also calculated from Eqs (2.2), (2.3), and (2.4a).

$$b_1 = \frac{-\alpha + te^{-j\theta}}{-\alpha t^* + e^{-j\theta}} \tag{2.5}$$

The transmission spectrum of the resonator can be expressed as,

$$T = |b_1|^2 = \frac{\alpha^2 + |t|^2 - 2\alpha|t|\cos(\theta - \phi_t)}{1 + \alpha^2|t|^2 - 2\alpha|t|\cos(\theta - \phi_t)} \tag{2.6}$$

where $t = |t|e^{j\phi_t}$ and ϕ_t is the phase change at the coupling section. The free spectral range, $\text{FSR} = \lambda^2/n_g L$ and the resonances occur when $(\theta - \phi_t) = m \cdot 2\pi$, where m is an integer,

$$T_{res} = |b_{1.res}|^2 = \frac{(\alpha - |t|)^2}{(1 - \alpha|t|)^2} \tag{2.7}$$

While the total circulating power is

$$|a_2|^2 = \frac{\alpha^2(1-|t|^2)}{1+\alpha^2|t|^2-2\alpha|t|\cos(\theta-\phi_t)} \tag{2.8}$$

From the above Equation (2.7), we can observe a critical coupling condition where transmitted power goes to 0 when the internal loss, α, are equal to the coupling loss, $|t|$. This critical coupling is introduced as perfect destructive interference between the transmitted field, ta_1, and the internal field coupled into the waveguide, κa_2. Figure 2.6 shows the transmission spectra for two different conditions. Notice when $|t|$ and α are equal, resonance features go to zero from Equation (2.7).

Another parameter of importance is the line width of the resonance which is called the full-width at half-maximum (FWHM). When the loss in the ring is negligible and coupling is symmetric, FWHM is expressed as [14]:

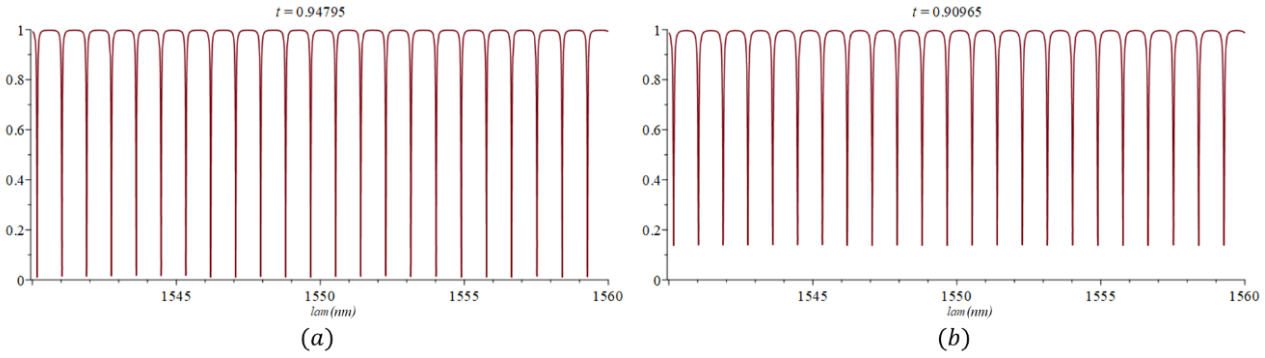

Figure 2.6. Transmission spectrum of a ring resonator of radius 200 microns under conditions (a) $t = 0.99a$ and (b) $t = 0.95a$, where the effective refractive index is 2.2 and group index is 4.8. The loss factor α is set to 0.95 for the simulation.

$$\text{FWHM} = 2\delta\lambda = \frac{\lambda^2}{\pi L n_{eff}}\frac{1-t^2}{t} \tag{2.9}$$

The next configuration (Figure 2.7) is the ring resonator add-and-drop configuration which consists of two straight waveguides and one ring resonator. When the light is injected, a fraction

goes through the coupling section and the rest couples to the ring cavity. The coupled light experiences a second symmetric coupling. At resonances, from Eqs. (2.6) and (2.8), the output power at the drop port ($|a_2|^2$) can be represented by, for resonances,

$$T_{res} = \frac{(1-|t_1|^2)(1-|t_2|^2)\alpha}{(1-\alpha|t_1 t_2|)^2} \tag{2.10}$$

When the two coupling sections are identical,

$$T_{\mathrm{AD.res}} = \frac{(1-|t|^2)^2\alpha}{(1-\alpha|t|^2)^2} \tag{2.11}$$

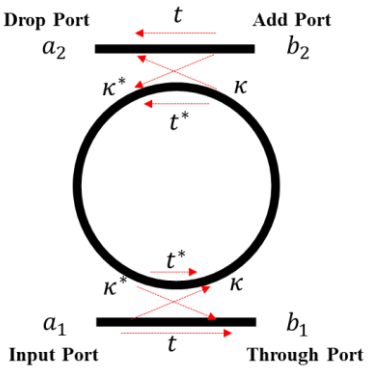

Figure 2.7 Add-and-drop ring resonator configuration

Quality factor Q, which is one of the essential parameters evaluating ring resonators, can be calculated from the previous equations. The Q factor is defined by the ratio of the operation wavelength to the FWHM.

$$Q = \frac{\lambda}{2\delta\lambda} = \frac{\pi n_{eff} L}{\lambda}\frac{t}{1-t^2} \tag{2.12}$$

Figure 2.8 shows the calculated transmission spectra of an add-and-drop configured ring resonator at the drop port for different quality factors. The resonance peak is fixed at 1.55 μm and

FSR at 25.6 nm. When the radius of the ring resonator is defined, FWHM varies as a function of quality factor Q. When Q increases FWHM reduces resulting in narrow peaks at resonance points.

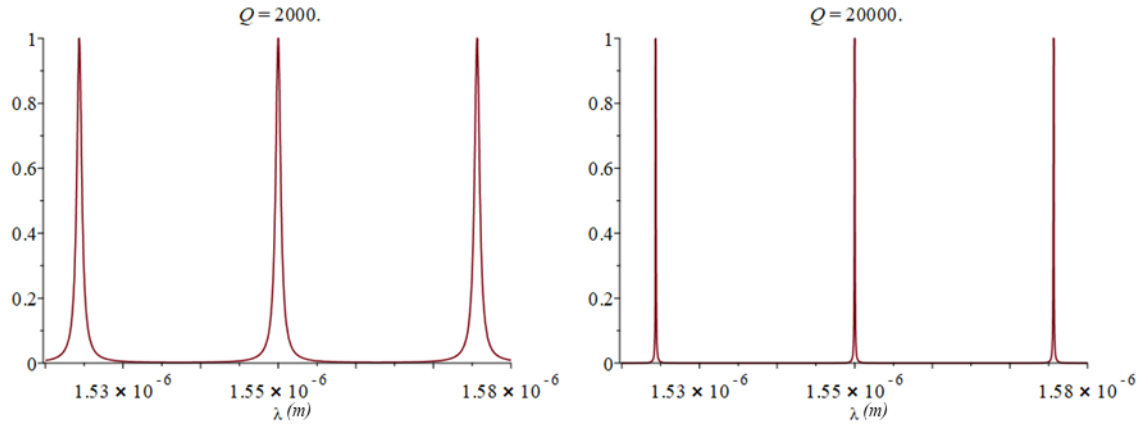

Figure 2.8 Calculated transmission spectra of the ring resonator at the drop port for different quality factors. High quality factor leads to sharp the resonance peaks, which allows more resonance to be captured.

2.3. Wavelength Division Multiplexer (WDM)

As discussed in the previous section, the transmission spectrum of a ring resonator has special characteristics at resonance. Note that due to the imperfection of fabrication, experimental results do not always meet expectations. This results in another control parameters to finely resolve the peaks [15]–[17]. However, only dimensional parameters are used in this paper to build a passive device. From the resonance condition, we can derive this master equation [18],

$$m\lambda_0 = n_{eff}^{\lambda_0} P \tag{2.13}$$

where P is the circumference of the ring, m (which is an integer) is the mode number, λ_0 is the central wavelength, and $n_{eff}^{\lambda_0}$ is the effective index at the given central wavelength. As we

introduce variations on the circumference of the ring resonator, ΔP, resonance wavelength shifted by $\Delta\lambda$. This relation can be expressed by,

$$m(\lambda_0 + \Delta\lambda) = n_{eff}^{\lambda_0+\Delta\lambda}(P + \Delta P) \tag{2.14}$$

From the two equations above (Eqs. (2.13) and (2.14)), we can derive an equation of central wavelength shift as a function of ring radius variation, shown as Figure 2.9. Derivation of the central wavelength shift equation is shown in detail (Eqs. (2.15) and (2.16)).

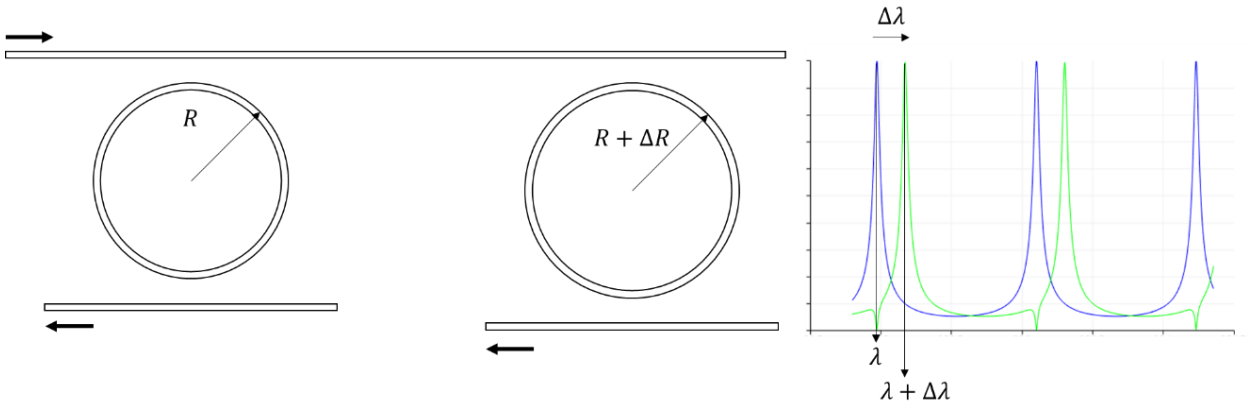

Figure 2.9 Configuration of central resonance wavelength resulted from ring radius variations (Left). As the perimeter of the resonator is changed, the central resonance wavelength is shifted.

$$1 + \frac{\Delta\lambda}{\lambda_0} = \frac{n_{eff}^{\lambda_0+\Delta\lambda}(P + \Delta P)}{n_{eff}^{\lambda_0} P} = \frac{\left(n_{eff}^{\lambda_0} + \Delta n_{eff}^{\Delta\lambda}\right)(P + \Delta P)}{n_{eff}^{\lambda_0} P} \tag{2.15}$$

where $n_{eff}^{\lambda_0+\Delta\lambda} = n_{eff}^{\lambda_0} + \Delta n_{eff}^{\Delta\lambda}$. As we rearranged the equation,

$$\Delta\lambda\left(\frac{1}{\lambda_0} - \frac{\frac{dn_e}{d\lambda}P + \frac{dn_e}{d\lambda}\Delta P}{n_e^{\lambda_0} P}\right) = \frac{n_e^{\lambda_0}\Delta P}{n_e^{\lambda_0} P} \tag{2.16}$$

where $\Delta n_{eff}^{\Delta\lambda} = \frac{dn_e}{d\lambda}\Delta\lambda$. As we neglect the small term,

$$\Delta\lambda \approx \frac{\left(\frac{\lambda_0}{P}\Delta P\right)}{\left(1-\frac{\lambda_0}{n_e}\frac{dn_e}{d\lambda}\right)} \tag{2.17}$$

Or,

$$\Delta\lambda \approx \frac{\lambda_0 n_{eff}\Delta P}{n_g P} \tag{2.18}$$

where $n_e - \frac{dn_e}{d\lambda}\lambda_0 = n_g$. The central wavelength shift ($\Delta\lambda$) can be obtained from the Eqs. (2.17) and (2.18). An ideal circuit of WDM can be realized from Lumerical INTERCONNECT by setting four different resonance wavelengths of each ring resonator (Figure 2.10).

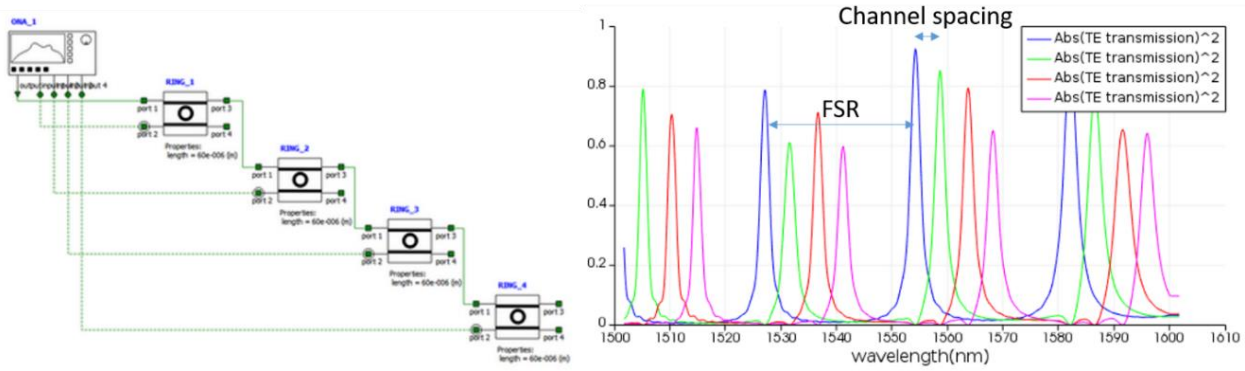

Figure 2.10 Four cascaded ring resonators perform as a de-multiplexer (Left). Transmission spectra of four cascaded ring resonators (Right). FSR is required to be wide enough to hold all four channels. Channel spacing is the distance between adjacent resonance peaks. Typically, uniformly distributed channel spacing is desirable.

2.4. Absorption Spectroscopy

From the transmission spectrum, one can extract characteristic parameters of the ring resonator [19], [20]. As we analyze the resonance of the transmission spectrum, we can obtain the group index, coupling coefficient, and propagation loss as a function of wavelength.

The calculated group index is found from a finite-element model of a single strip waveguide. The total absorption coefficient a (or a_T) for the propagation through the ring is then characterized by the relation, $\alpha = e^{-a_T L/2}$. The total absorption under analytes can be expressed by [6], [7]

$$a_T = a_I + \Gamma a_A \tag{2.19}$$

where a_I is the intrinsic waveguide loss, a_A is the absorption from the analyte, and Γ is the confinement factor which represents how much light is interacting with the cladding material.

Instead of using ring resonator structures, simple waveguides can be substituted for the cost of short effective lengths which reduces the performance of the sensor. However, it is advantageous to use waveguide channels since they exhibit better tolerance for detection capabilities. While the ring resonators require a high-resolution detection scheme, waveguides allow us to have a lower resolution detection scheme which is done by the WDM system. In which case, the absorption spectrum can be measured from the equation below.

$$aL = 10 \log_{10} \frac{I_1}{I_2} \tag{2.20}$$

where I_1 is the intensity of light transmitted through a ring resonator without analytes and I_2 is the light intensity when analytes are applied. The waveguide length L is contacting with the chemical solution. Therefore, when output intensity spectra I_1 and I_2 of the chip are measured on a fixed length of the waveguide (L), the absorption (a) can be calculated through Equation (2.20).

3. SIMULATION AND FABRICATION

In this section, we will discuss simulation methodologies and results. Lumerical software is used for the simulation. For the ring resonator sensor, characteristics of ring resonator are analyzed from the Lumerical program. For the WDM, a series of ring resonators are analyzed at the same time to make cascaded ring resonators which act as a WDM device. Fabrication procedures and design layouts are presented and discussed in the following subsection.

3.1. Ring Resonators

In order to verify the theoretical calculations, computer simulation is performed on RR silicon devices. Simulation software can analyze in various ways: Modal analysis, 2.5D Variational FDTD (varFDTD) Propagation, and 3D Finite-difference time-domain (FDTD). Modal analysis examines the structure of a waveguide and obtains the information on dispersive properties and field amplitudes at each mode, while varFDTD simulates the propagation of the light.

Transverse Magnetic (TM) mode is considered to enhance interaction between the waveguide and the analyte. Lumerical Software is used to analyze mode profiles and dispersion properties of straight and bent waveguides. Finite-difference time-domain (FDTD) method is adopted to calculate S-parameters of coupling sections using Lumerical FDTD Solutions. Dispersive properties (effective index, group index, dispersion, and loss) are extracted from Lumerical MODE Solutions and added to Lumerical INTERCONNECT to simulate structures as a whole device.

Figure 3.1 shows a ring resonator circuit for simulation. It consists of two bus waveguides and two directional couplers and two bent waveguides. Four parameters (effective index, group index, loss, and dispersion) of each waveguide (straight waveguide and bent waveguide) are extracted from MODE Solutions. A waveguide which is 500 nm wide and 220 high is used for the simulation. the radius of curvature of the ring and the length of the straight waveguide are input parameters. The S-parameter is extracted from 3D FDTD simulation where the same structure of the waveguide and ring radius is applied.

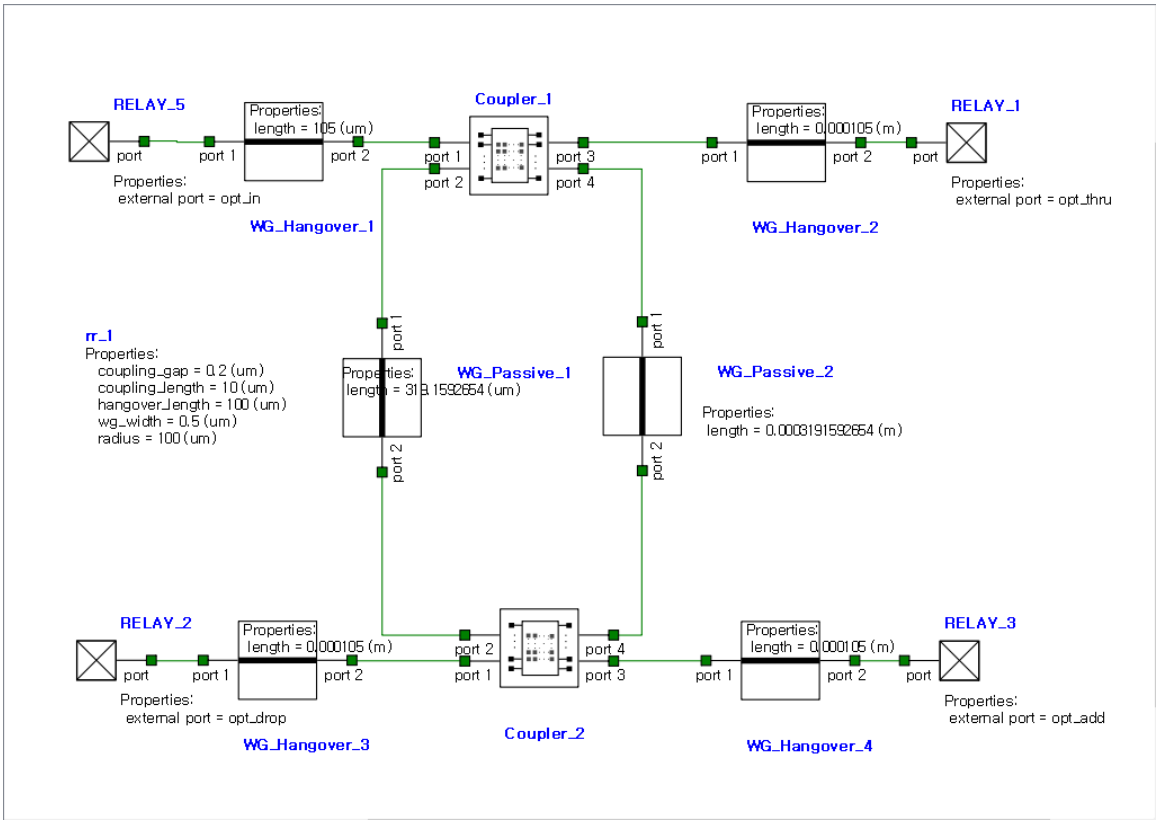

Figure 3.1 Waveguide-based ring resonator circuit in INTERCONNECT.

A ring resonator simulation is given to compare the simulation results with experimental results. Lumerical Compact Model Library (LCML) is used as a reference for this simulation. The transmission spectrum of the ring which has a 50 µm radius of curvature and a coupling gap of 0.2 µm is shown as Figure 3.2.

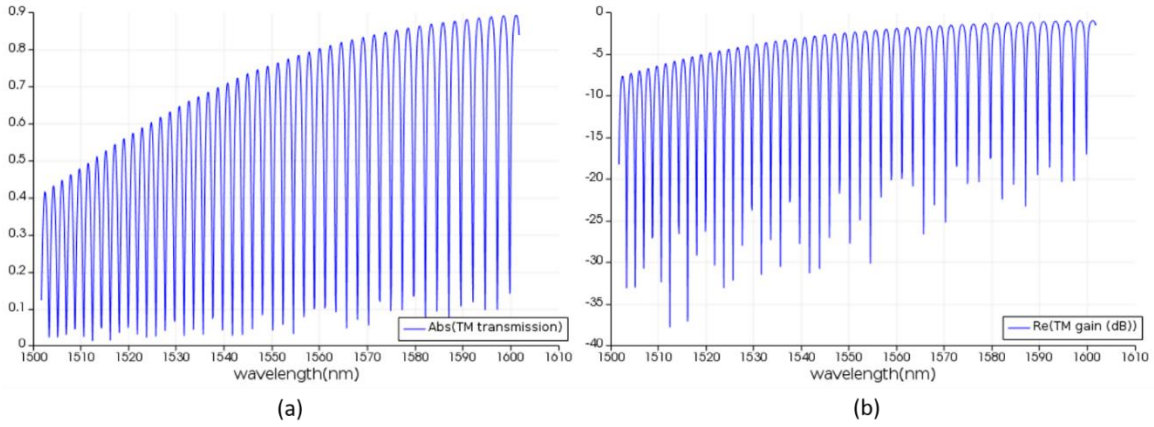

Figure 3.2 Transmission spectra of a ring resonator of 50 µm radius with no coupling length, and coupling gap of 0.2 µm. This spectral information is simulated by Lumerical INTERCONNECT. (a) Normalized transmission spectrum and (b) log scale transmission spectrum are given.

Some of the fabricated features of the ring resonators are shown and the measurements of the structures are given. Figure 3.3 shows a coupling region between a ring and a bus waveguide. The left image shows its structures before the etching process and the right one presents its features after the etching process. Etching itself was performed with low fabrication error. However the E-beam lithography itself which determines the resolution of the devices made a relatively significant error compared to the etching procedure. Although we designed our ring resonator to have a 200

nm gap and waveguides of 500 nm wide, but Figure 3.3 shows about 10% fabrication error in these particular features.

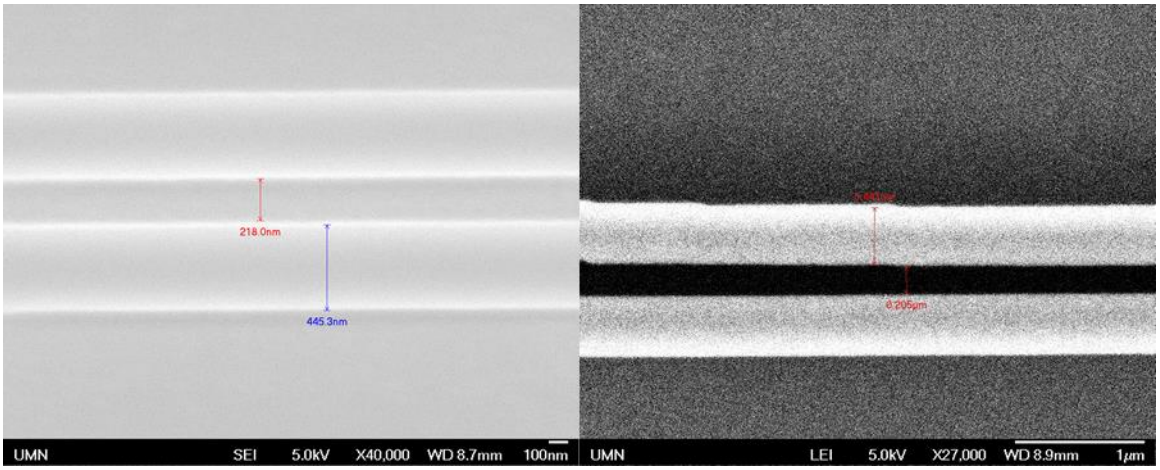

Figure 3.3 Image of gap between a ring and a bus waveguide before the etching procedure (Left) and after the etching (Right). Images are provided by the University of Minnesota.

3.2. Wavelength Division Multiplexer (WDM)

Figure 3.4 shows a simulation workflow for the WDM design. Instead of using the circuit design in the previous section, we made a whole device simulated in 3D FDTD software. After the simulation, S-parameters based on the design can be extracted from transmission spectra. Then, we varied the diameter of the ring to introduce a central wavelength shift and repeated the same simulation process to estimate the new S-parameters. After obtaining all the parameters, a complete device performance can be observed through Lumerical INTERCONNECT.

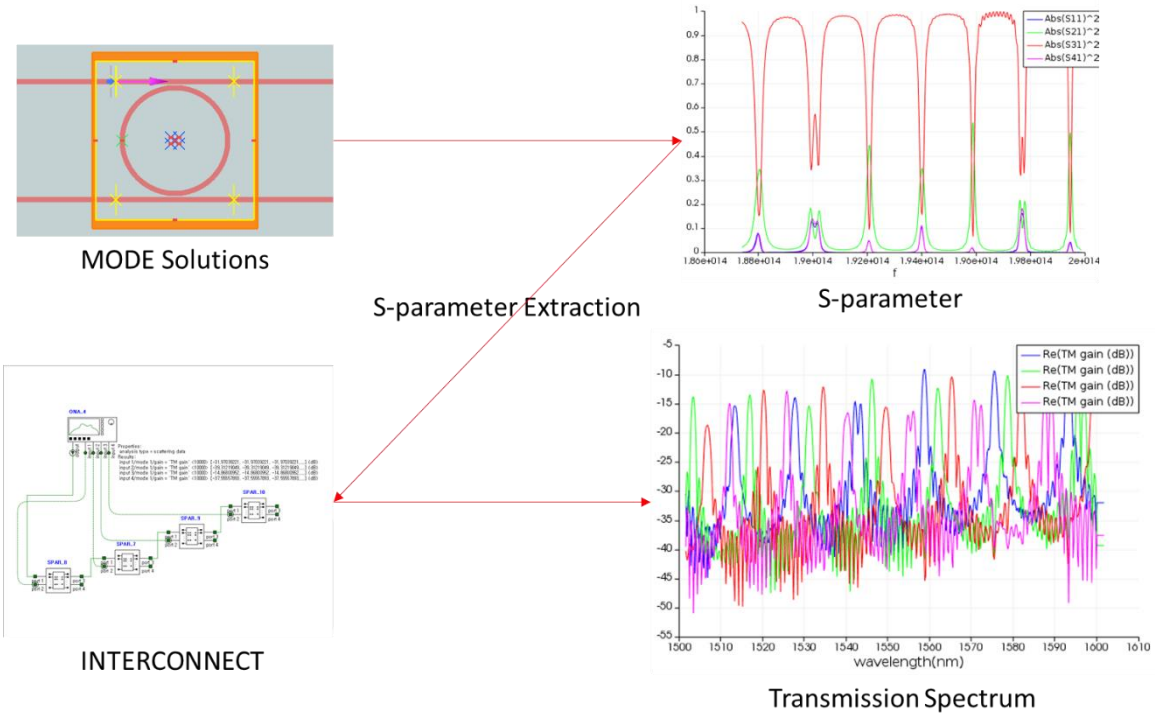

Figure 3.4 WDM simulation workflow. Lumerical FDTD Solutions is used for each individual device, and Lumerical INTERCONNECT is used to simulate the whole WDM device.

One can calculate the central resonance wavelength shift from Equation (2.18). For the simulation, a strip waveguide having 500 nm width and 220 nm height is considered. Group index and effective index are calculated from the Lumerical MODE Solutions using the specified waveguide cross section. Figure 3.5 shows transmission spectra of the two different sizes of ring resonators having a radius of 5 μm and 8 μm each. To make 4 channels WDM, channel spacing should be one-fourth of the free-spectral range. From equations of FSR and channel spacing, desired radius variations can be calculated. Ring resonators with radius of 5 μm and 8 μm yield FSRs of 16 nm and 10 nm respectively. A radius change of 40 nm leads to channel spacing of 4

nm for the 5 μm ring resonator, and 35 nm of variation leads to 2.5 nm channel spacing for the 8 μm ring resonator.

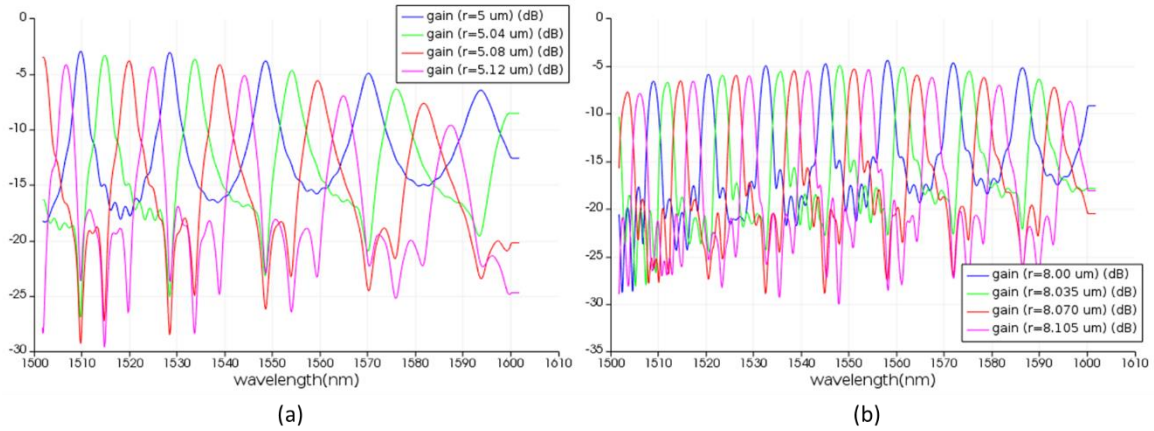

Figure 3.5 Transmission spectra of four channels WDM with a radius of (a) 5 μm and (b) 8 μm in a log scale. A 5 μm ring resonator shows 40 nm increase step to make uniformly distributed channel spacing, and 8 μm ring resonator produces 35 nm increase.

3.3. Grating Coupler

Light coupling into a photonic circuit from a fiber is a challenging problem, due to their size contrast. While a fiber core is typically about 10 microns in diameter, a photonic waveguide has sub-micron width. In order to address this problem, edge coupling is used with low insertion loss [21]. However, this approach can only be used at the edges of a chip. Also, the alignment to couplers requires significant efforts especially when it comes to alignments of multiple input and output sources which is required for a WDM device.

Surface coupling is another solution to the problem that uses grating couplers [22]–[24]. It is advantageous over the edge coupling in that it does not require a lensed fiber and edge polishing. As mentioned in the previous paragraph, alignments of multiple sources are enabled by using the grating couplers and fiber array units. In this way, we can reduce the footprint of the design and alignment work.

We studied a fully etched grating coupler design, which is cost-efficient and simplifies a design over a shallow etching grating in that it can be fabricated using a single exposure step while shallow etching requires two etching steps. However, fully etched gratings create a strong back reflection into the waveguide due to the large refractive index contrast in the grating region. Sub-wavelength structures have been introduced to enhance coupling efficiency and minimize the back reflection at the same time [25], [26].

We verified designs of a reported paper using Lumerical FDTD Solutions and accepted their design parameters to fabricate the grating coupler [26]. For the TE mode, the grating coupler shows 55% of coupling efficiency, which meets their report and fits our design (Figure 3.6). For the TM mode, it shows about 45% of coupling efficiency (Figure 3.7). Note that, as we discussed earlier in the section, we employ TM mode for the sensing.

Unfortunately, due to the limitation on fabrication process sub-wavelength gratings cannot be etched. Figure 3.8 shows two SEM images of a grating coupler before and after etching. While the gratings are patterned with the E-beam lithography, they cannot be resolved after the etching. Finally, we cannot help adopting shallow etched grating couplers. Shallow etching is more

typically used for grating couplers because it requires less resolution limit. However, it makes the wafer to be processed two times at different etching depths which increases the fabrication time and cost.

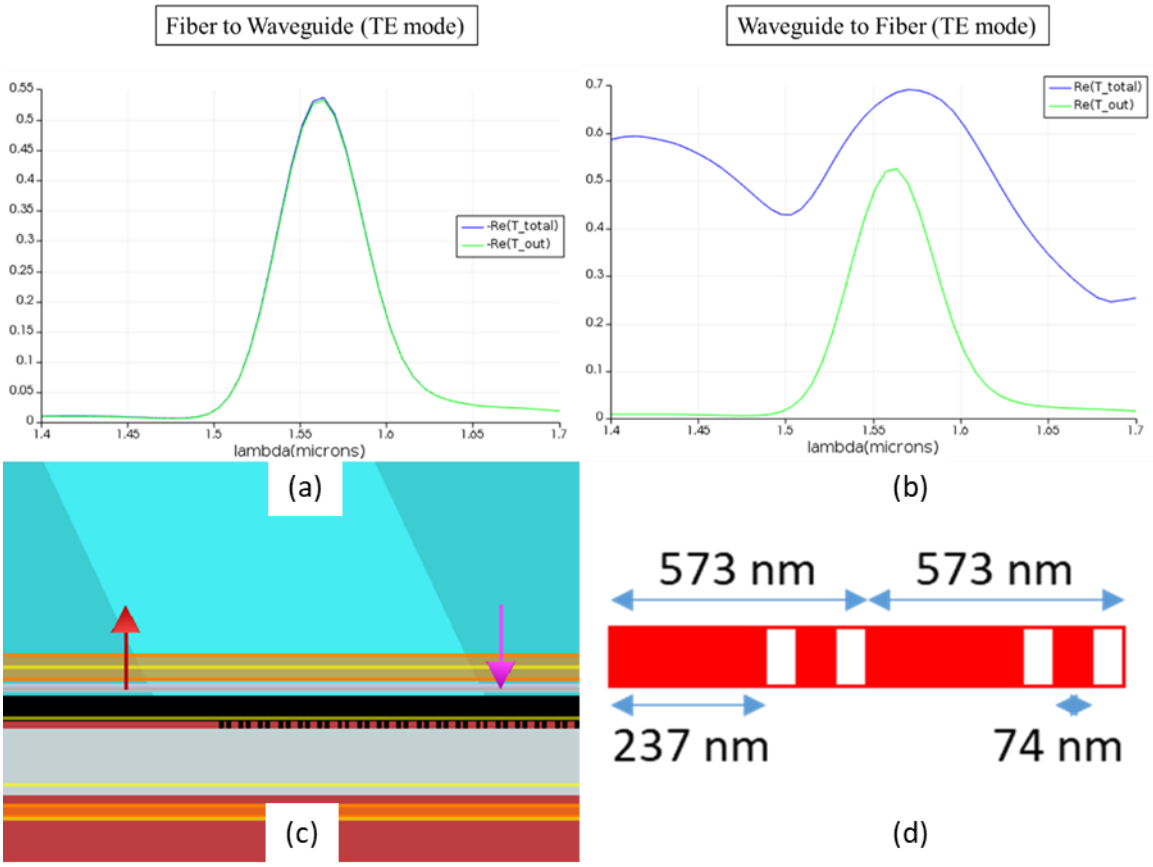

Figure 3.6 Transmission spectra of the grating coupler on TE mode (a) from a fiber to a waveguide and (b) vice versa, (c) The simulation window, and (d) grating geometry.

Instead of accepting previous fabrication, we designed grating couplers based on our design parameters. Since we have a fiber array unit which is polished at an angle of 8°, we set our incident angle, θ, at the same angle. We designed for both TE and TM mode to compare the resulting

measurements. The central wavelength, λ, is set to 1.55 μm. The Bragg condition to calculate the grating period can be expressed by [23],

$$n_{air} \cdot \sin\theta = n_{eff} - \frac{\lambda}{\Lambda} \tag{3.1}$$

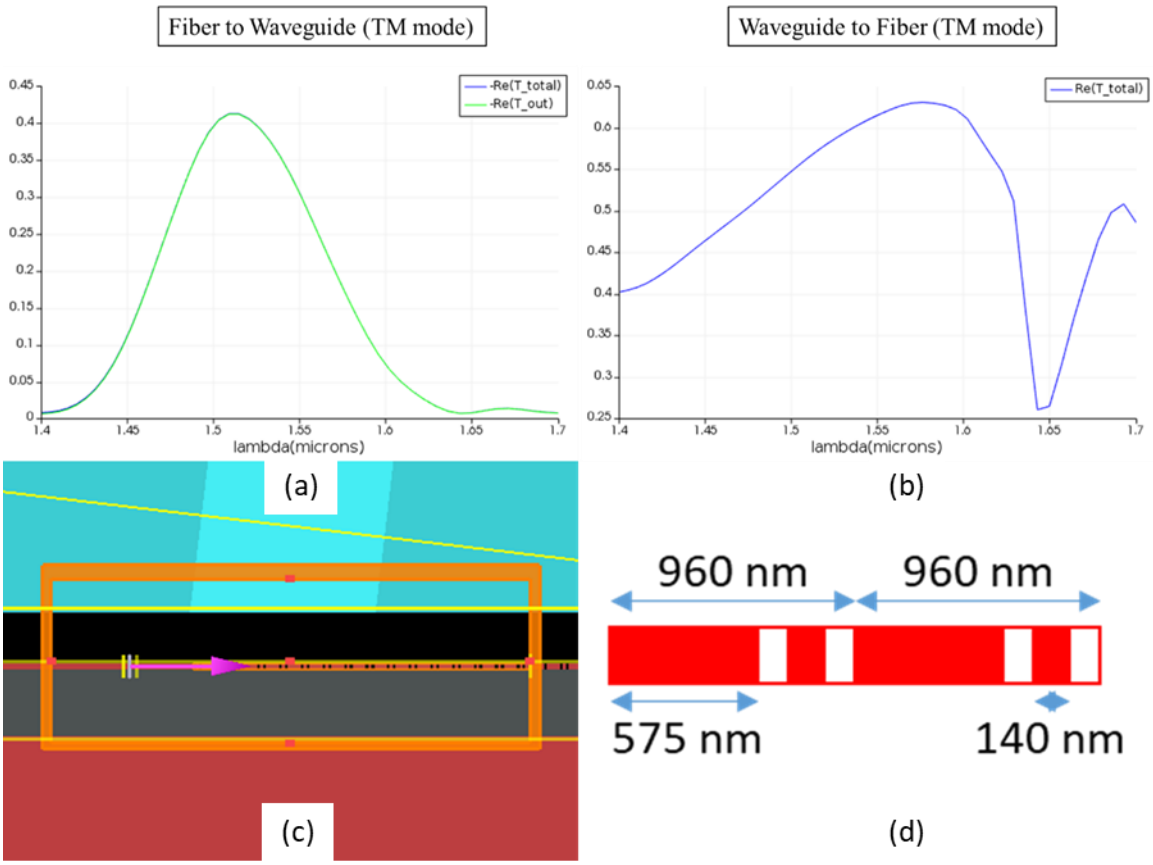

Figure 3.7 Transmission spectra of the grating coupler on TM mode (a) from a fiber to a waveguide and (b) vice versa, (c) the simulation window and (d) grating geometry.

where n_{air} denotes the refractive index of air, n_{eff} denotes the effective index of the grating region, and Λ denotes the grating period when the cladding is air. The effective index of the grating, n_{eff}, is expressed as $(n_{eff,f} + n_{eff,s})/2$, where $n_{eff,f}$ is the effective index of the strip

waveguide and $n_{eff,s}$ is the effective index of the shallow etched strip waveguide. The devices layer is 220 nm thick and shallow etch depth is 70 nm. The fill-factor (defined as a ratio of the shallow-etched groove width to the grating period) is set to 50%. From all the above information, we can calculate the grating periods of TE and TM grating couplers.

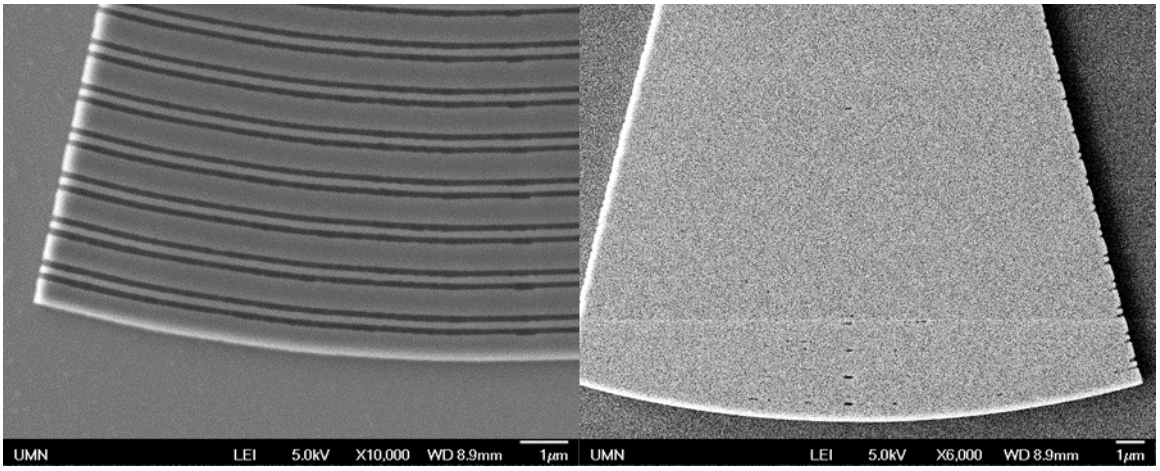

Figure 3.8 Left: SEM image of the grating coupler before the second etch. Right: SEM image of the grating coupler after the second etch. Images are provided by the University of Minnesota.

The simulation results from the calculated parameters for TE mode are shown as Figure 3.9. The grating period is 610 nm, the fill factor is 50%, and the angle of incidence is 8°. The results show the coupling efficiency of about 50% for both directions, from the fiber to chip and from the chip to fiber, which exhibits similar efficiency compared to the fully etched grating couplers. Figure 3.10 presents the simulation results from the calculated parameters for TM mode. The grating period is 960 nm, the fill factor is 50%, and the angle of incidence is 8°. About 50% of the TM mode power is coupled from fiber to the waveguide and 60% from the waveguide to chip.

3.4. Fabrication

Silicon photonic waveguides requires sub-micron resolution to confine the fundamental optical mode properly. Typical CMOS manufacturing process cannot be used to fabricate silicon photonics chips. E-beam lithography is chosen due to its fine resolution. A 4″ SOI wafer with 525 µm of total thickness, 1.1 µm thick insulator, and 250 nm thick Silicon layer is prepared for the patterning. The wafer is first cleaned in Piranha solution of H2SO4:H2O2 2:1 for 10 minutes to eliminate surface contaminants and to promote adhesion of HSQ resist to the surface, possibly through surface oxide formation. After that, the wafer is rinsed with DI water, followed by a dry step with a nitrogen gun.

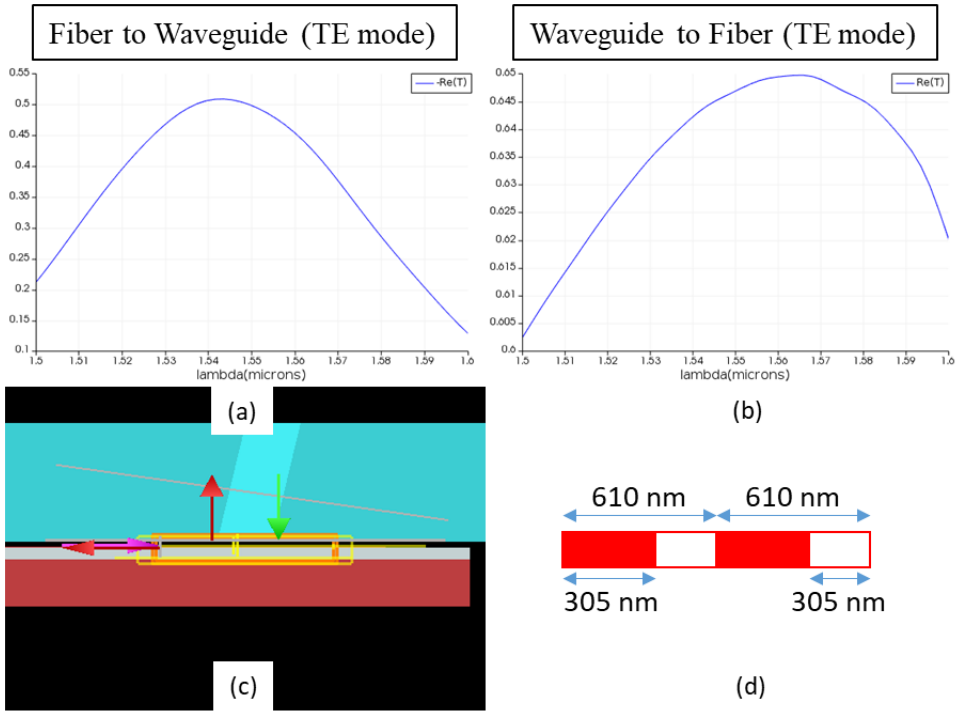

Figure 3.9 Transmission spectra of the grating coupler on TE mode (a) from a fiber to a waveguide and (b) vice versa, (c) the simulation window, and (d) grating geometry.

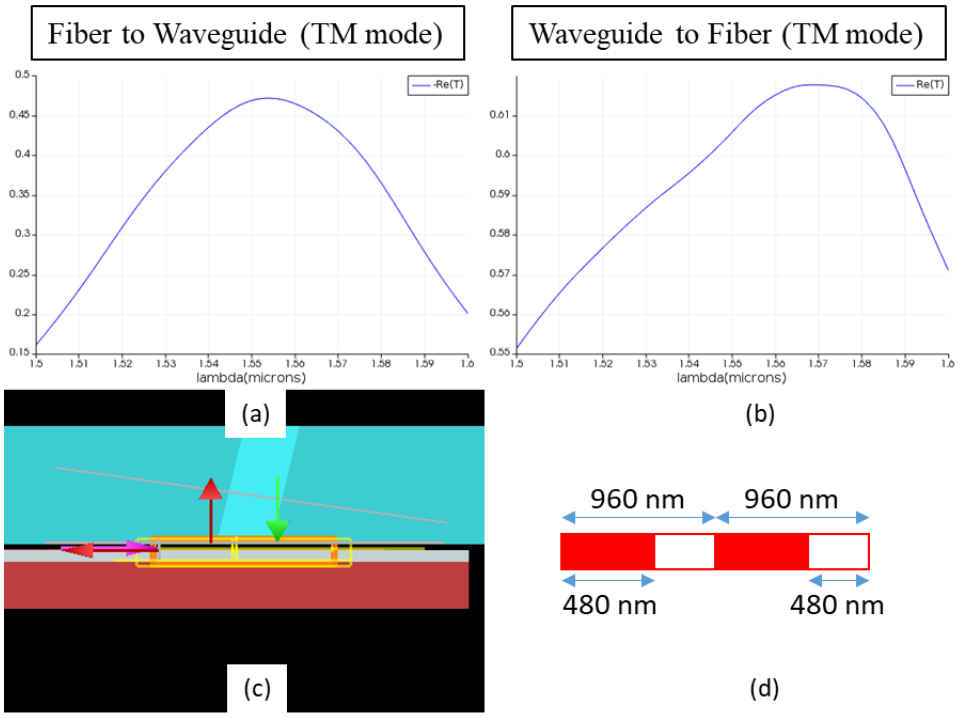

Figure 3.10 Transmission spectra of the grating coupler for a TM mode (a) from a fiber to a waveguide and (b) vice versa, (c) The simulation window, and (d) grating geometry.

In order to build our devices, we collaborated with the Nano center of the University of Minnesota for their E-beam fabrication capability. Before the wafer is coated with a photoresist, it is baked for dehydration at 180 ℃ for 5 minutes on a hotplate and then cooled for 1 minute. The PR 8% HSQ (1 part Dow Corning's FOX-16 (16%) resist diluted with 1 part MIBK) is spin-coated at 3000 rpm for 30 seconds to produce a 200 nm film. After it soft-baked at 80℃ for 4 minutes on a hotplate, the wafer is exposed with Vistec EBPG 5000+ e-beam lithography system which has 1 nm fracture, 10 nm beam step size. An applied voltage of 100 kV produces 30 nA electron beam and base dosage of 1800 μC/cm2. The wafer is developed in 319 Developer (1 to 5% TMAH based) for 3 minutes. In the first minute, most of the wafer will be clear. After an additional 2 minutes will clear optical input regions and spiral regions where patterns are denser, and hence negative

resist may have produced halo features around the regions. The development time can go up to 4 minutes if additional dense regions need to be cleared of their corresponding halos. Afterward the wafer is rinsed with DI water, following dry-step with a nitrogen gun.

In order to etch the top silicon layer (250 nm thick), PlasmaTherm Deep Trench Etcher and the 'cnf-14-v' recipe developed at Cornell for etching nano features are used. Etch rate for silicon is 200 nm/minute, the etch rate for HSQ resist is 70 nm/min, and the etch rate for thermal oxide is 35 nm/min. The wafer is etched for 1.25 minutes minimum to clear the 250 nm of silicon, but generally a 10% over-etch is employed to ensure all top silicon is gone, so it will take a total time of 83 seconds. The whole process is arranged in Table 3.1.

3.4.1. Layout

We designed four different die designs and 18 dies in total, as shown in Figure 3.11. Design #1 contains basic alignment units and WDM units. Design #2 is basically the same design as design #1 except for the grating coupler. While design #1, #2 and #4 are configured for the TM mode, design #2 is designed for TE mode. Design #3 contains ring resonators and racetrack resonators. Three different radii of curvature are considered: 50 μm, 100 μm, and 200 μm, in addition to different gaps between the bus waveguide and the ring: 100 nm and 200 nm. Design #4 contains spiral waveguides and combinations of ring resonators and WDMs.

Table 3.1 Process flow for Silicon Photonic device fabrication

Process Step	Equipment/Chemical/ material/thickness	Wafer profile
Initial SOI Wafer		
PR Coating	8% HSQ resist (200 nm)	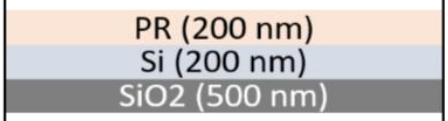
Waveguide Lithography and Development	Vistec EBPG 5000+ e-beam lithography and 319 Developer	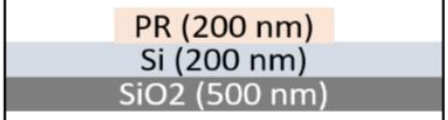
Waveguide Etch	PlasmaTherm Deep Trench Etcher (200 nm)	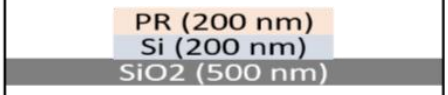
Remove PR	Rinsed with DI water	
Coupler PR Coating	8% HSQ resist (200 nm)	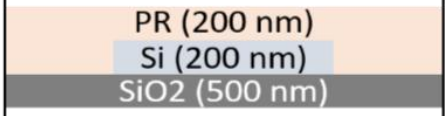
Coupler Lithography and Development	Vistec EBPG 5000+ e-beam lithography and 319 Developer	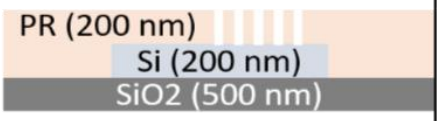
Grating Etch	PlasmaTherm Deep Trench Etcher (70 nm)	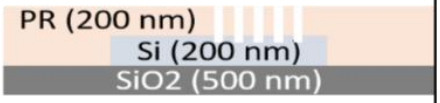
Remove PR	Rinsed with DI water	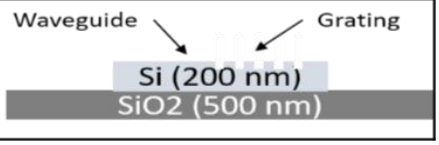

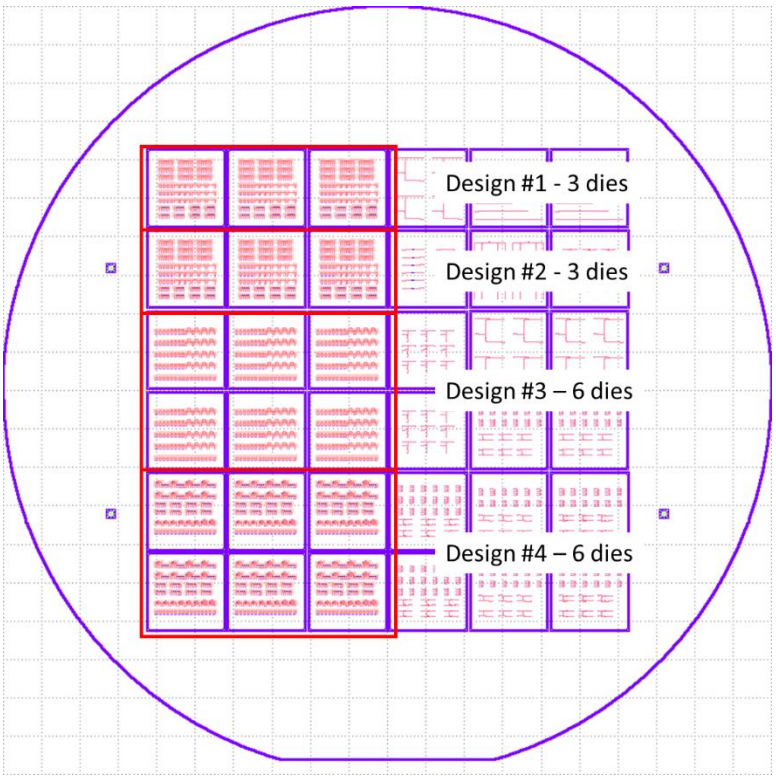

Figure 3.11 The complete wafer layout.

In order to enhance design efficiency and reliability, we used E-beam Package Design Kit (PDK) which is an open source design library made by Lukas Chrostowski and his team at University of British Columbia [23]. For the layout software K-Layout is selected. E-beam PDK offers basic structures, such as waveguides, ring resonators, grating couplers, and so on, and also a number of design examples which consist of the basic structures. These libraries allow us to use pre-coded libraries. These also prevent us from making unexpected design errors due to its pre-designed and pre-coded structures.

Figure 3.12 shows the design layout of design #1. There are 7 different device layouts and 38 devices in total. Device #1 to #5 are basically alignment mark units with different waveguide

lengths. We can also study the loss from propagation of the light along each waveguide. Device #6 and #7 are WDMs with different FSRs. While device #6 is designed so that FSR is set to 16 nm, FSR of device #7 is set to 10 nm as we discussed at the WDM section. These WDM devices have 4 channels which are equal distance to produce a uniform spacing. In order to satisfy these requirements, a coupling-gap and ring-geometry are properly chosen from calculations and the corresponding simulations are discussed in the simulation section.

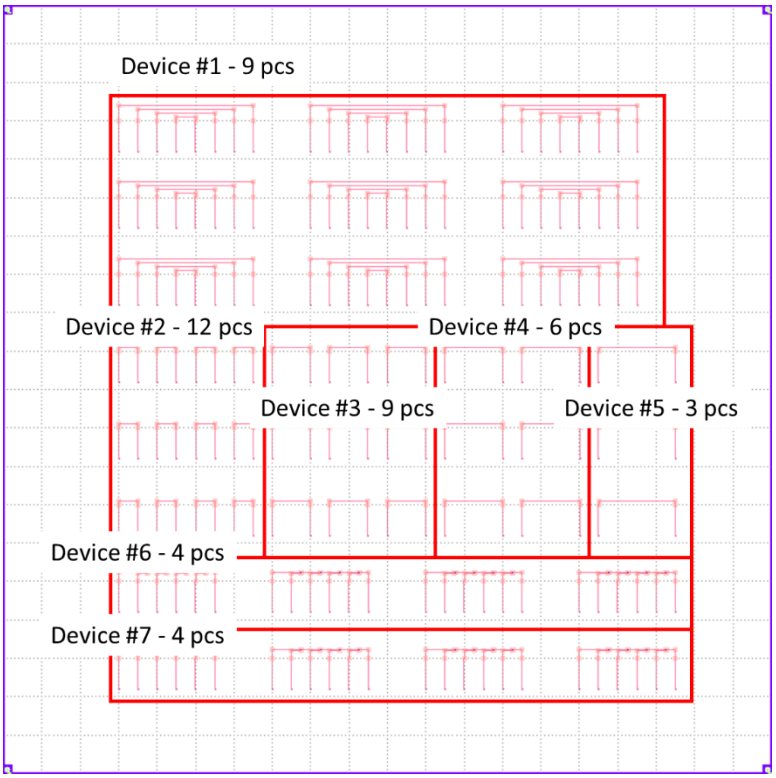

Figure 3.12 Design #1 Layout contains seven different devices.

Figure 3.13 shows a zoom-in image of the device #1 layout. Grating couplers are separated by 250 μm which is the spacing of the array fiber core for the alignment purpose. Each grating coupler

is about 400 µm long and 12 µm wide. Waveguides are separated by 50 µm at least in order to prevent cross talk between straight waveguides which causes optical losses in the measurements.

Figure 3.14 shows four different devices from Design #1. They are employed for the purpose of the alignment check. The only difference between these devices is their propagation lengths. Using these devices we can figure out the optical loss of a given structure.

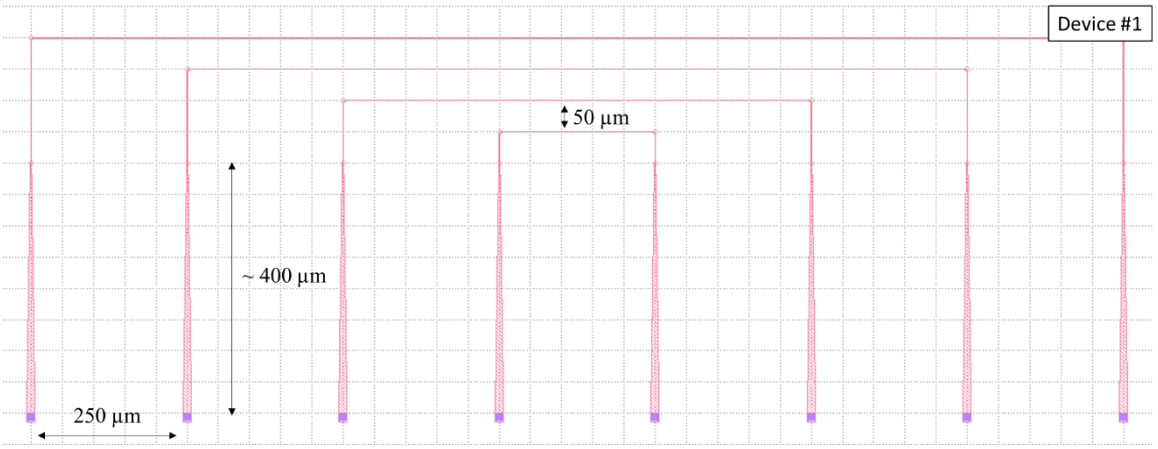

Figure 3.13 Device #1 layout shows a fiber alignment check circuit.

Figure 3.15 and Figure 3.16 show design layouts of the WDM devices. There are two types of WDM devices with different FSR and channel spacing. One has a FSR of 16 nm and channel spacing of 4 nm, while the other has FSR of 10 nm and channel spacing of 2.5 nm. The radius of ring resonator is expected to be 5 µm to make an FSR of 16 nm. We want the channel spacing to be one-fourth of the FSR that is 4 nm. From the Equation (2.18), we can calculate the desired radius variation which is 40 nm. Ring resonator of radius 8 µm has an FSR of 10 nm. The radius variation of 35 nm makes the central wavelength shift to be 2.5 nm, which is one-fourth of the

FSR. The gap between the bus waveguides and the ring resonators are 200 nm. Each grating coupler is 250 µm apart so that a fiber array unit can be aligned instead of individual fibers.

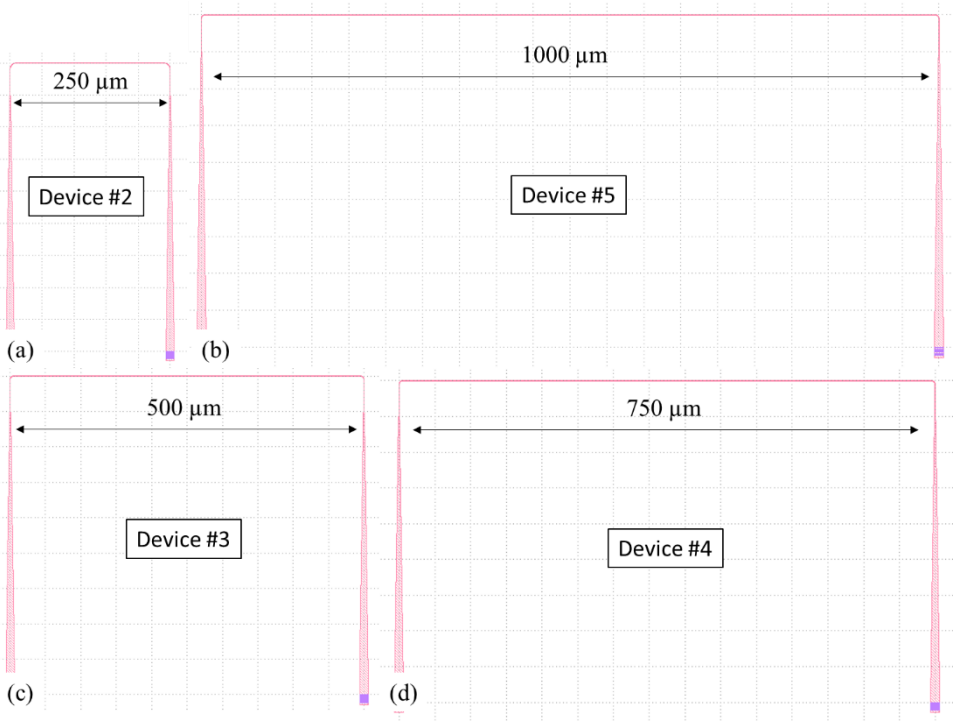

Figure 3.14 Device #2, #3, #4, and #5 are designed in order to check alignment of each circuit.

Figure 3.17 shows the design layout of design #2. Device #8 to #13 are various geometry of ring resonators. Device #14 to #19 are the racetrack resonators. While the ring resonators have no coupling length between the bus waveguides and the ring resonators, but the racetrack resonators have 10 µm coupling length.

Figure 3.18 and Figure 3.19 show devices from #8 to #13. Device #8 has a ring radius of 50 µm and the coupling gap of 100 nm. Device #9 has a ring radius of 100 µm and the gap of 100 nm.

Device #10 has a ring radius of 200 µm and gap of the same separation. The radius of the ring of device #11 is 50 µm and its gap is 200 nm. The ring radii of device #12 and #13 are 100 µm and 200 µm, respectively and their gap is 200 nm.

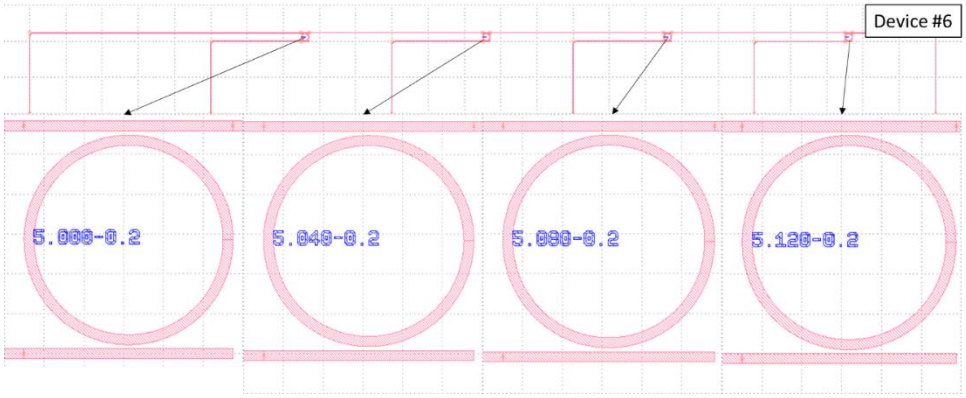

Figure 3.15 Device #6 layout shows a WDM device (Unit in microns).

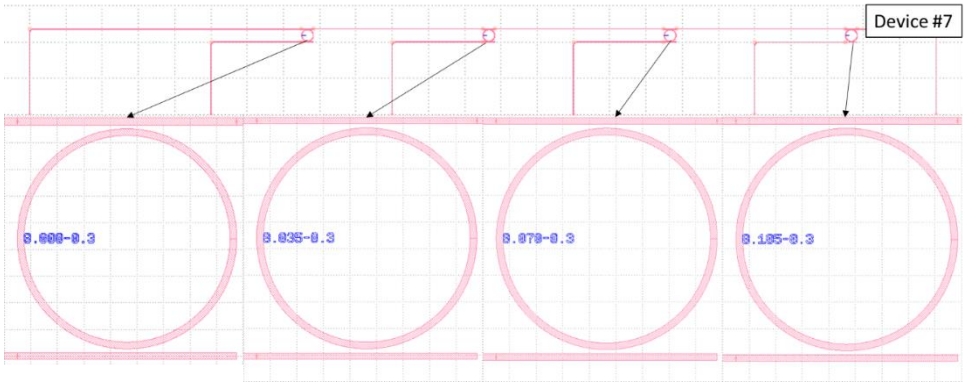

Figure 3.16 Device #7 layout a WDM device (Unit in microns).

Figure 3.20 shows two different designs of ring resonators. While the top picture has no coupling length, the lower picture has a coupling length of 10 µm. This coupling length allows the light to be coupled from an input to an output.

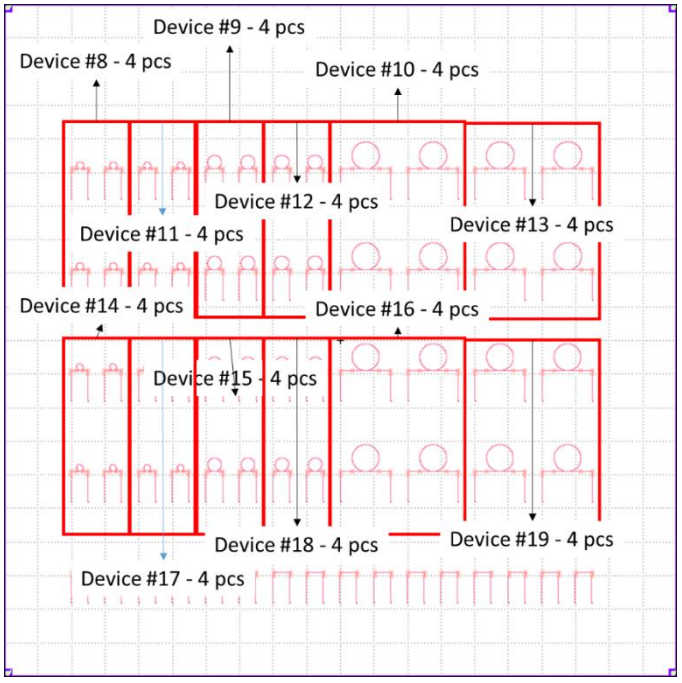

Figure 3.17 Design #2 Layout. Radii of ring resonators and gaps between a ring and a bus waveguides are varied. Various combinations of them are designed.

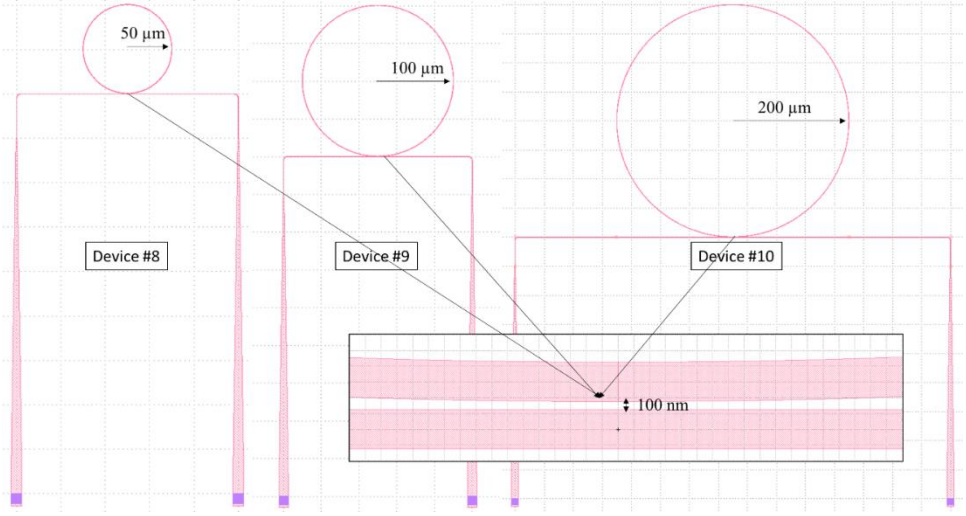

Figure 3.18 Device #8, #9, and #10 layout. All devices have the same coupling gap but a different radius of curvature.

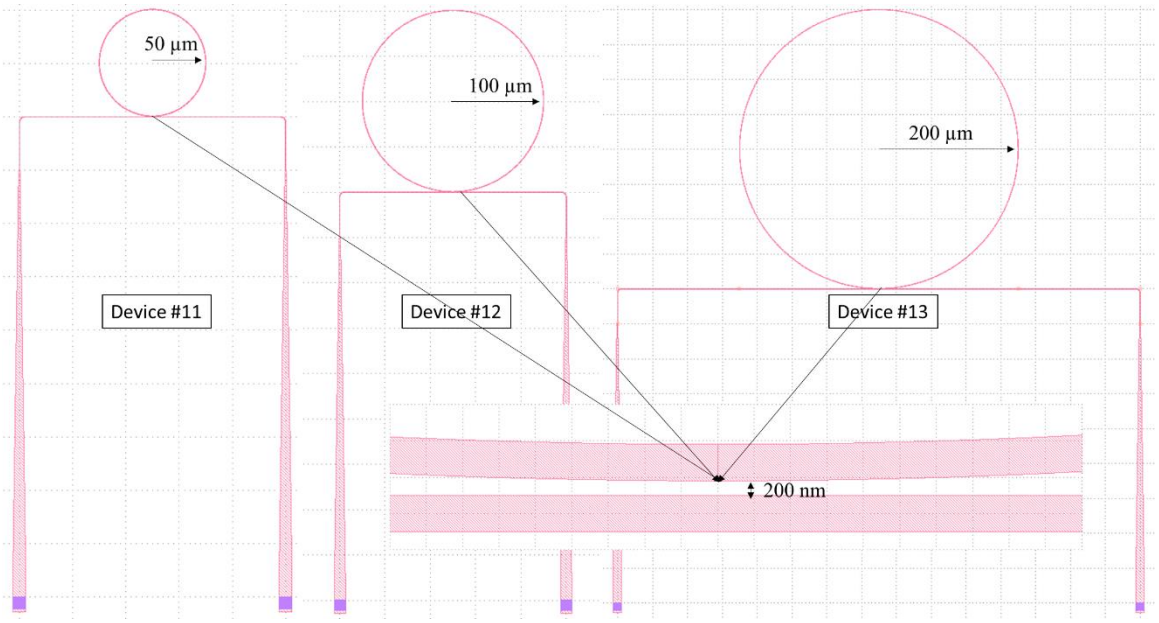

Figure 3.19 Device #11, #12, and #13 layout. All devices have the same coupling gap but a different radius of curvature.

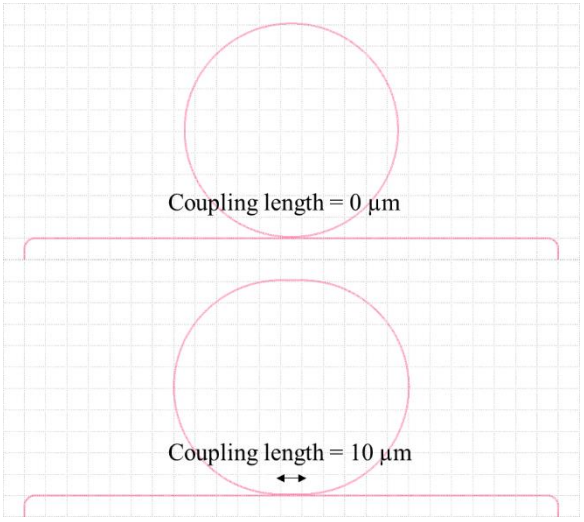

Figure 3.20 (Top) ring resonator and (Bottom) racetrack resonator configurations.

Figure 3.21 shows devices from #14 to #19, which are racetrack ring resonators. Devices from #14 to #16 have 10 µm coupling length and a gap of100 nm. The ring radii of resonators are 50

μm, 100 μm, and 200 μm for device #14, #15, and #16, respectively. Devices from #17 to #19 have 10 μm coupling length and a gap of 200 nm. The ring radii of resonators are 50 μm, 100 μm, and 200 μm for device #17, #18, and #19, respectively.

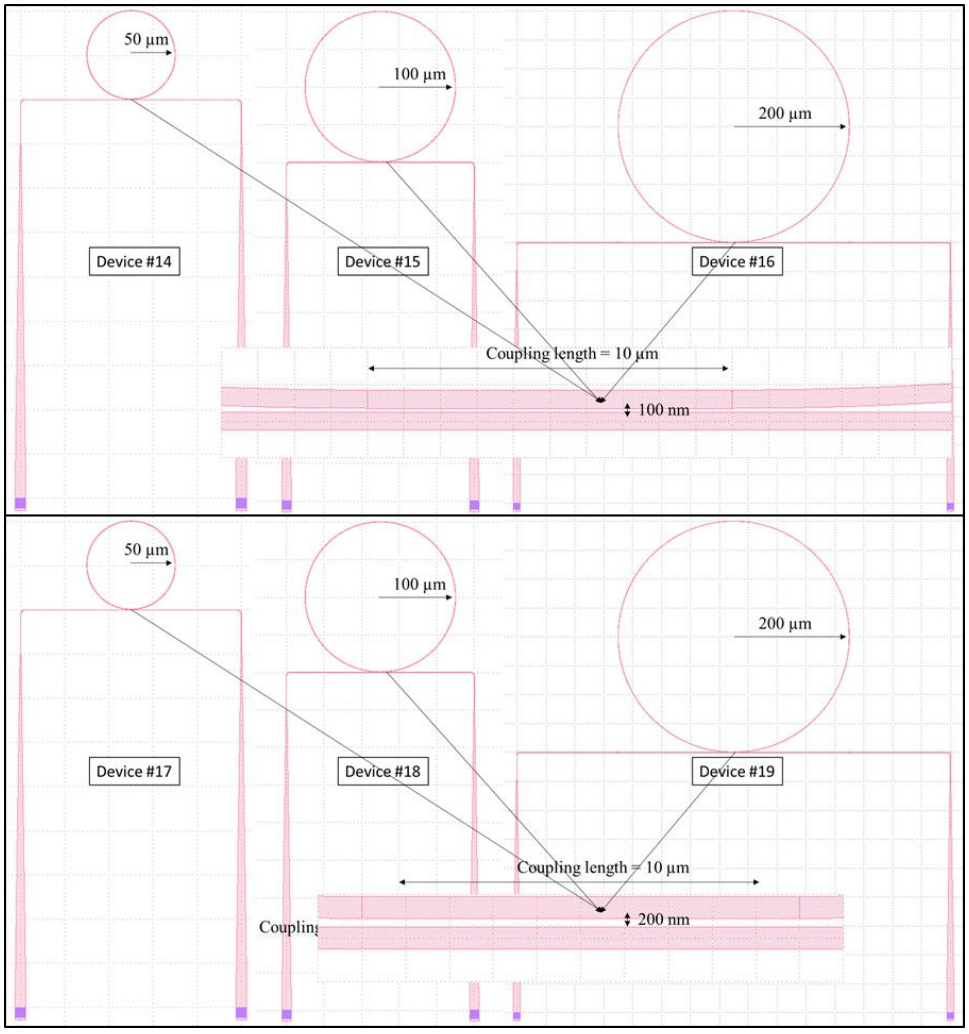

Figure 3.21 Device layout #14 - #19. All devices have the same coupling length but a different radius of curvature and coupling gap.

Figure 3.22 shows the design #3 layout. Spiral waveguides are designed through #20 to #22. Device from #23 to #26 are combinations of ring resonators and WDMs. Devices from #27 to #30 consists of spiral waveguides and WDMs.

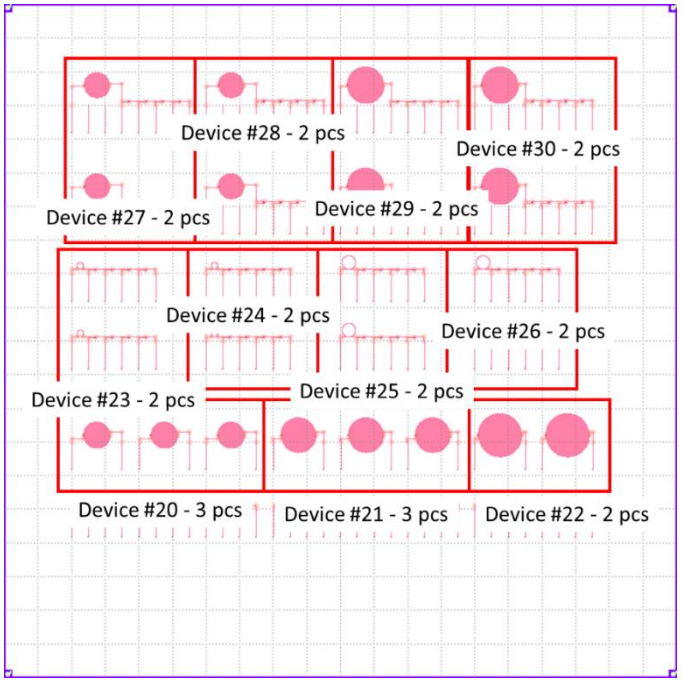

Figure 3.22 Design #3 Layout. Spiral waveguides and ring-resonator based WDM sensor circuits designs.

Spiral waveguides with different waveguide lengths are designed and presented in Figure 3.23. The lengths of the spiral waveguides are 1 cm, 2 cm, and 3 cm. The spiral waveguides are designed in order to verify waveguide propagation losses.

Figure 3.24 and Figure 3.25 show two different types of sensors. These devices will be used to verify and compare the results from device #27 - #30. Ring resonator and spiral-shaped waveguide sensors were designed. Bus waveguides and ring resonators are separated by 0.1 µm. Radii of ring

parts are 50 µm and 100 µm. Device #23 consists of device #8 and device #6. Device #24 is made out of device #8 and device #7. Device #25 is comprised of device #9 and device #6. Device #26 is designed using device #9 and device #7.

Figure 3.23 Device #20, #21, and#22 layout (Unit in microns). Total length of each spiral waveguide is shown within the figure.

Figure 3.25 shows four different devices. Device #27 is the combination of devices #20 and device #6. Device #28 is designed with device #20 and device #7. Device #29 employed #21 and device #6 in it. Device #30 is made out of device #21 and device #7.

Figure 3.26 shows zoom-in images of the layouts of grating couplers for TE and TM modes. Gratings are designed to be 12 µm long which is the width of the grating so that the grating region takes 12x12 µm² area [27]. Gratings for TE mode consist of 20 separate corrugations, while for TM mode 12 separate corrugations. The taper is 400 µm long in order to couple the light from a 12 µm wide waveguide to a 450 nm wide waveguide with a low loss. Their coupling efficiencies are presented in Figure 3.9 and Figure 3.10. Roughly 50% efficiency is calculated for the grating

couplers at their central wavelength peaks. However, as the fabrication errors and alignment error are introduced, it is expected to have a much less coupling efficiency in practice.

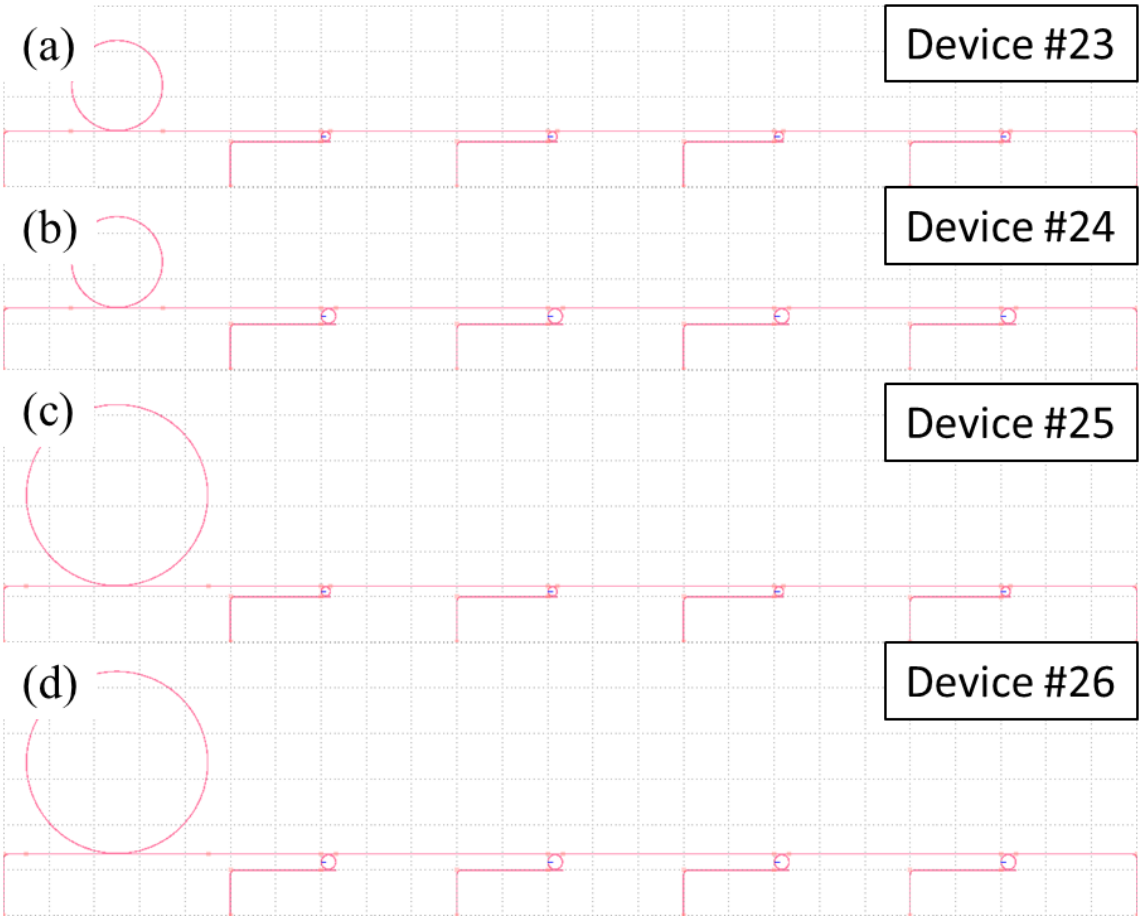

Figure 3.24 Device #23, #24, #25, and #26; In all these devices a ring resonator and a WDM device are combined to serve as a sensor.

3.4.2. Wafer Thinning

Before the SOI wafer was sent to the University of Minnesota for the E-beam lithography based fabrication, we thinned the silicon layer of the SOI which was initially 2µm thick. Figure 3.27

shows thickness maps of SOI wafer before thinning and after thinning. The overall roughness of the SOI wafer did not improve, but it got worse. The variation between the minimum and the maximum thickness was about 300 nm before the thinning while the variation after thinning was about 400 nm. Due to this large variation, we chose to use some selected region of the wafer. The right image of Figure 3.27 presents our target region using a red dotted line. The target region has an average thickness of 250 nm with a variation of 10% based on our estimation.

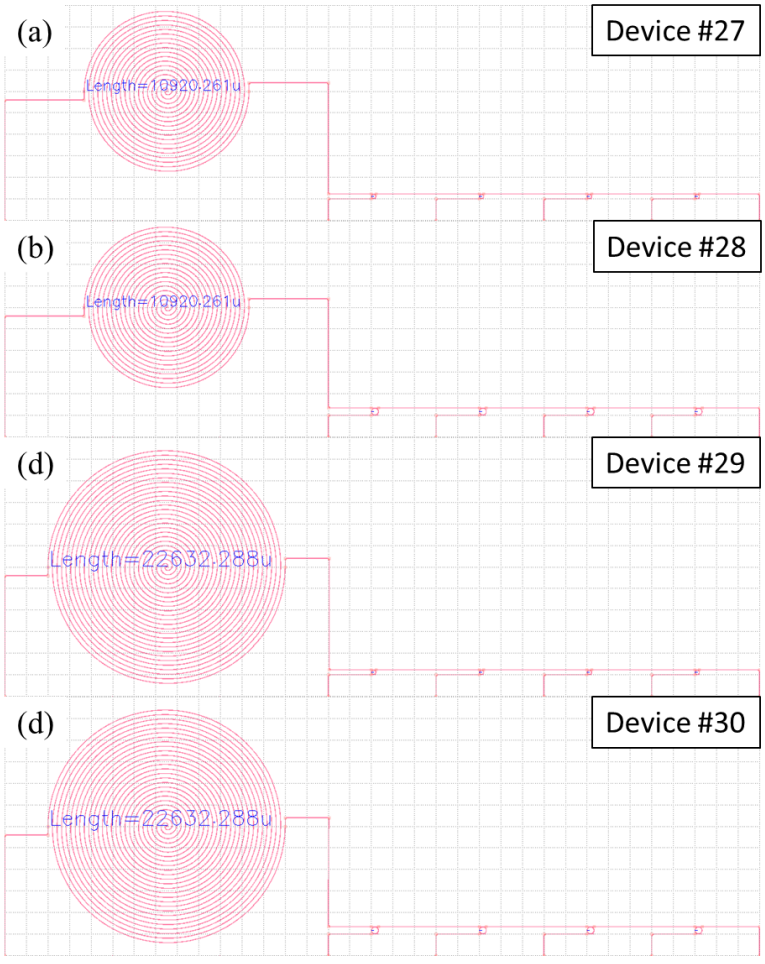

Figure 3.25 Device #27, #28, #29, and #30 layouts. A spiral waveguide and a WDM device are combined in order to build a sensor.

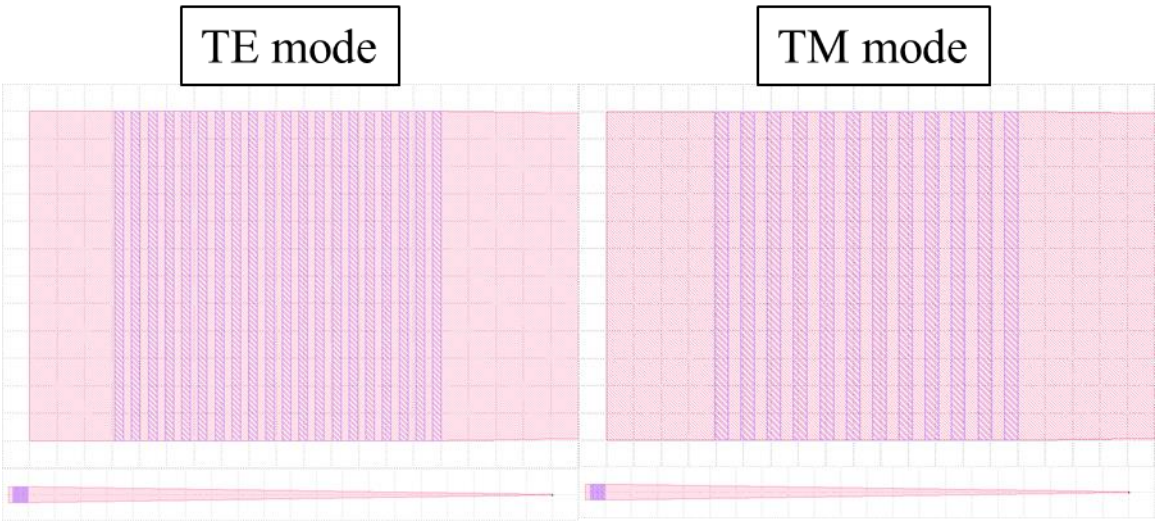

Figure 3.26 Grating coupler layouts for both TE and TM modes. (Left) zoom-in image of the gratings and zoom-out image of the grating coupler of TE mode, (Right) zoom-in image of the gratings and zoom-out image of the grating coupler of TM mode

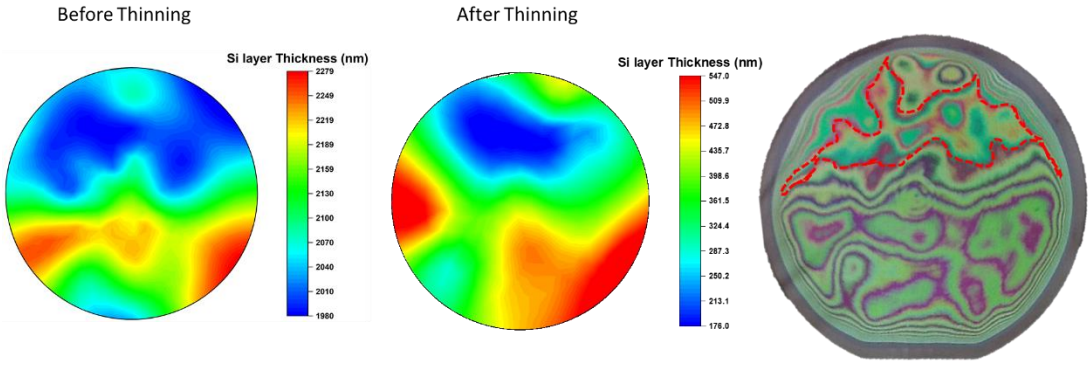

Figure 3.27 Silicon layer thickness maps on SOI wafer (Left and center). Image of the SOI after thinning (Right).

To thin the silicon thickness of the SOI wafer, we grew thermal oxide on the SOI surface. Newly grown silicon dioxide layer consists of 46% of the silicon on the top surface of the wafer

and 54% of the newly built silicon dioxide. We set the temperature of the furnace to 1000 ℃. From the typical parameters, we calculated the estimated time for the oxidation. After the oxidation growth oxide layer was removed from the surface using Buffered Oxide Etch (BOE). This process is repeated until we have the desired layer thickness before sending the wafer to the University of Minnesota.

Figure 3.28 shows our device layout on the wafer. Each chip is 10x10 mm² size. The region surrounded by red curved lines is the area which has the desired layer thickness. So, the devices are intentionally located within this region. In this way, we expected to have more working devices. The same devices are also duplicated on the other regions for fabrication.

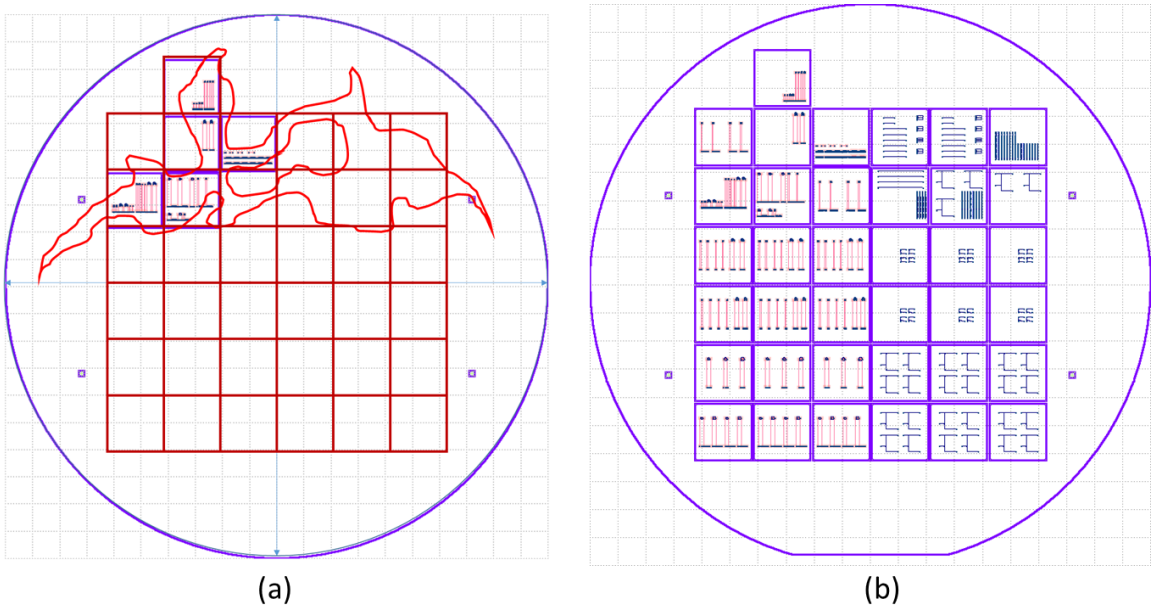

Figure 3.28 Red line represents the target region which has the desired thickness. (a) Devices are located based on the silicon layer thickness. (b) Devices over the whole wafer.

Unfortunately, the devices were not able to be patterned at an etching step. Especially, all the corrugations of the grating couplers were etched away although they were successfully patterned by the e-beam lithography. Due to the fabrication failure of the first wafer, we repeated the thinning process to prepare a new wafer. This wafer has a device layer of 500 nm and very small surface roughness (Figure 3.29). While the first wafer had over 500 nm thickness roughness, this wafer only varies within 20 nm. Therefore, we designed the device layout over the whole wafer.

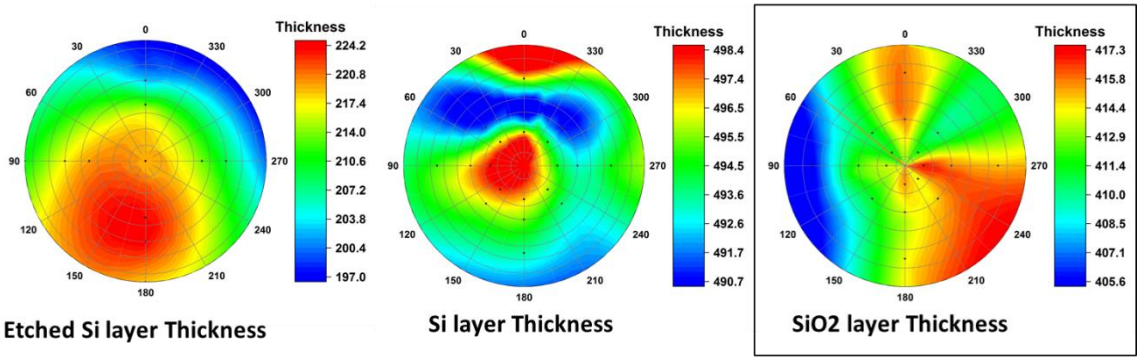

Figure 3.29 Silicon layer thickness maps on the new SOI wafer.

4. EXPERIMENT AND RESULTS

In this section, we will discuss the experimental setups. Since WDM Photonic Integrated Circuits (PICs) need several input/output (I/O) channels, we need to properly align the input and output grating couplers to I/O optical-fibers. However, aligning several fibers in one chip at the same time could lead to severe alignment problems such as physical interferences between fibers and setups. Therefore, instead of using several fibers, a fiber array unit is employed in order to align the grating couplers at the same time.

A three-axis stage is used to adjust a sample platform. We installed a coarse resolution stage, having approximately 10 μm resolution and a fine resolution stage having approximately 1 μm resolution. A coarse alignment stage is first adjusted then the fine resolution stages are controlled to find the best alignment. An optical-fiber array unit is controlled by a rotation stage, a 3-axis stage, and a tilt stage to properly align the fiber array to the I/O grating couplers on the chip. The fiber array is connected to an input source and a detector to measure the data.

4.1. Input and Output (I/O) Setup

As our integrated ring resonator-based WDM has 4 channels, a proper alignment methodology is required to input and output the source and the data from the devices. When the WDM of 4 channels is integrated on a chip, we need at least 4 outputs and one input totally 5 I/O components. However, due to limited physical spaces on an alignment stage, proper alignments of 5 I/O components at the same time are extremely difficult, especially when we need to align them manually. Therefore, the fiber array unit is introduced to reduce difficulties of alignment and

improve the experimental procedures. We used a fiber array of 8 channels which has more channels than our number of I/O units. Furthermore, to couple the light in and out of a chip, we used a set of grating couplers to reduce the overall footprint of the devices while maintaining desired coupling efficiency. Grating couplers of less than 5dB loss at a central wavelength of 1550 nm are used [22]–[24], [26].

Figure 4.1 shows a customized design of a fiber array holder which is used to hold the fiber array unit. Figure 4.2 presents a measurement setup. To build the setup, 3 axis translation stage is used for the chip placement. Additional camera system and the fiber array also are controlled by different 3-axis translation stages. A rotational stage is attached to the fiber array holder to adjust the angle of incidence which plays an important role in coupling the light to the silicon device.

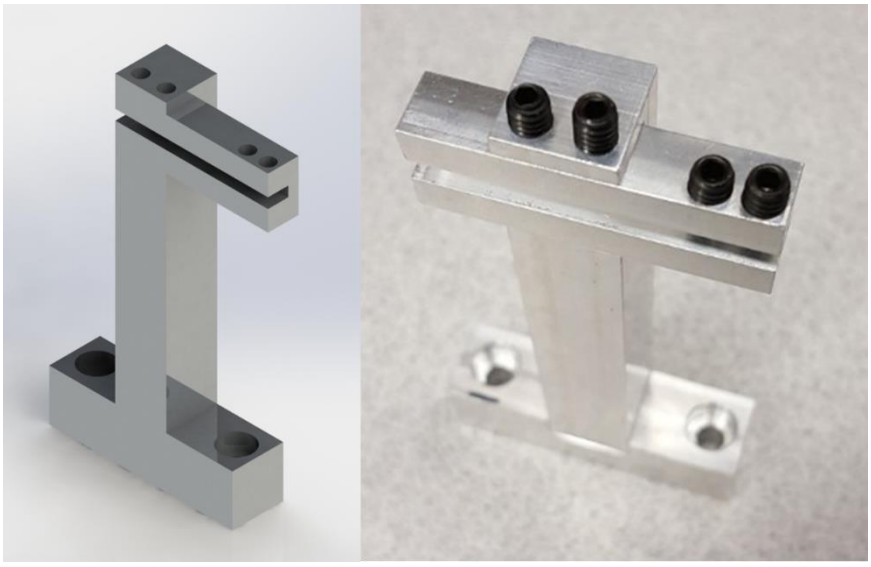

Figure 4.1 Fiber array unit holder. (Left) 3D CAD model and (Right) its machined aluminum part.

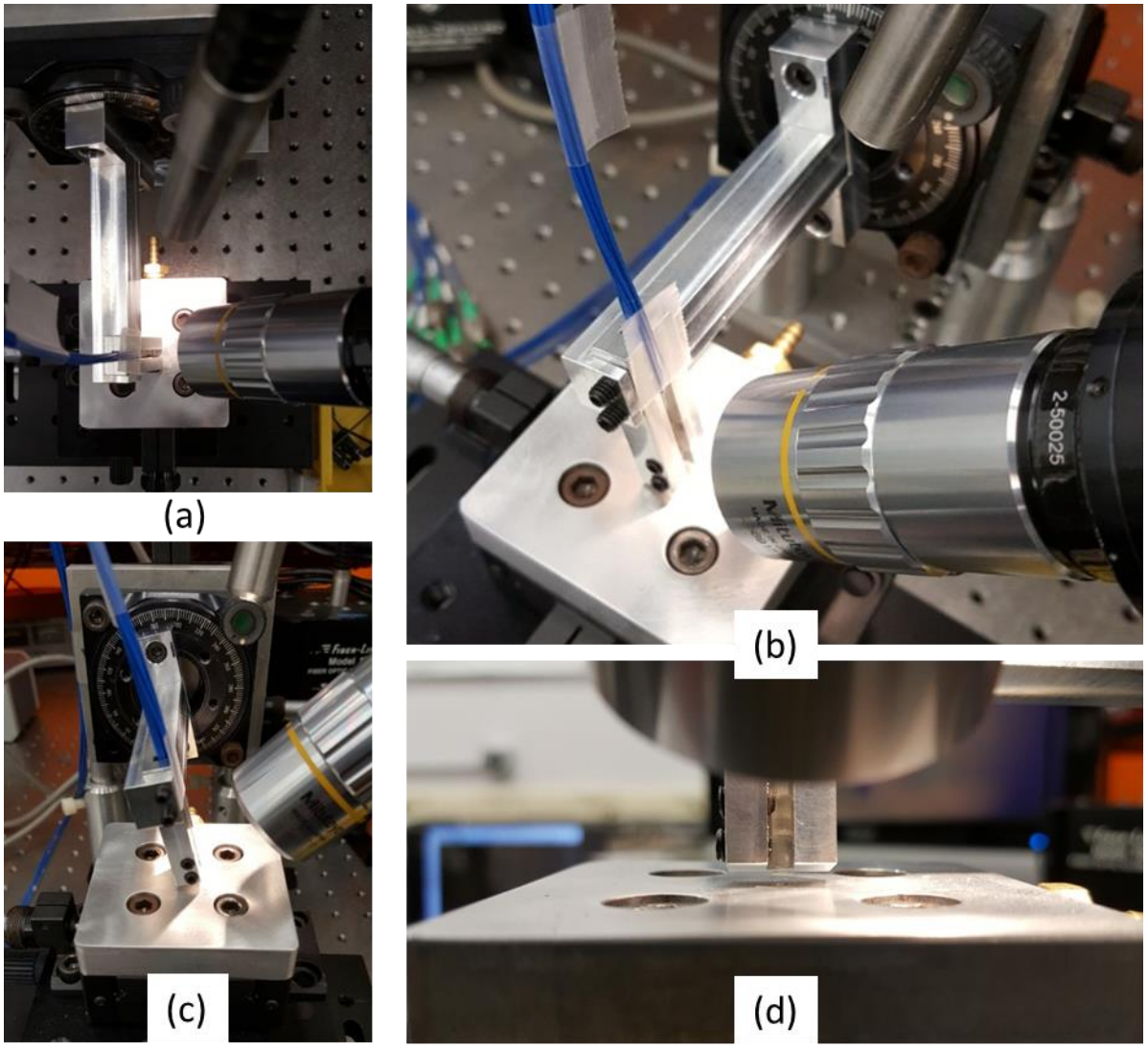

Figure 4.2 Measurement setup using a fiber array, (a) top-view, (b) angled-view, (c) side-view, (d) and the front-view are shown

4.1.1. Viewing Camera

Aligning the fiber array to the grating couplers requires tedious and delicate work due to their small footprint. The resolution limit, magnification, and Field of View (FOV) are considered

important properties of the viewing cameras. Resolution limit is important in that it determines the sensitivity of a stage control which is 1 μm in our experiment. Magnification should be large enough to discriminate grating couplers and waveguides. FOV is also expected to be wide enough to capture the fiber array unit and the silicon WDM simultaneously.

Figure 4.3 shows our selected camera lenses (Navitar) for the setup. Table 4.1 presents the specifications of each camera. For the upper camera, a resolution limit of about 1 μm is chosen due to the resolution-limit of our 3-axis translation of stage. FOV is wide enough to capture all the fiber array cores, while narrow enough to zoom-in on one or two fiber array cores. The lower camera is only used to align the distance between the fiber array and the chip. So, fewer magnification lenses are chosen in that the loss is negligible when they are separated by around 10 μm [24], [28].

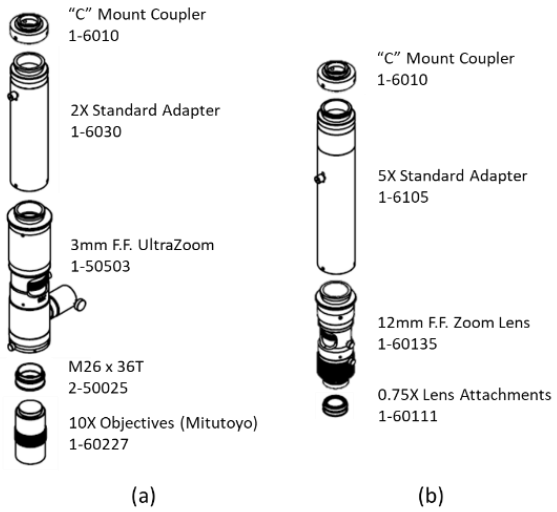

Figure 4.3 (a) Top-view camera system diagram, (b) side-view camera system diagram. Model numbers are shown.

Table 4.1 Specifications of the camera setup

	Upper Camera	Lower Camera
Magnification	Up to 66.63x (5.54x – 66.63x)	Up to 16.88x (2.63x – 16.88x)
Numerical Aperture	0.28	0.053
Resolve Limit (μm)	Up to 1.19	Up to 6.28 (19.60 – 6.28)
Working Distance (mm)	33	113
Field of View (mm)	3.05 – 0.47	1.44 – 0.12

4.1.2. Optical-Fiber Array

A fiber-array stage is used to help align the optical fiber cores with the grating couplers on the chip. Compared to a single-fiber or two-fiber alignment setup, a fiber array is not always a good way to couple the light. However, when multiple ports are required such as WDM, fiber-array is a reasonable choice to make the system work efficiently. As our WDM is designed for 4 channels, we need at least 5 ports (including the input port). For this reason, a fiber-array of 8 channels is adopted. To maintain a specific mode, in our case a TM-mode, polarization maintaining (PM) fiber-array is chosen with a typical pitch of 250 μm.

A fiber array unit is purchased from Precision Micro-Optics (FPFA-10208221312). Figure 4.4 shows the fiber-array dimension parameters. Our fiber array unit is 3.5 mm wide, 1.5 mm high, and 10 mm long with a quartz housing material. The pitch accuracy is less than 0.5 μm. Figure 4.5 shows an image of the fiber-array via the setup camera. We can clearly see the eight fiber cores in

the fiber array. A type of polishing angle is selected to make the separation between the chip and the fiber core as small as possible in order to prevent power leakage.

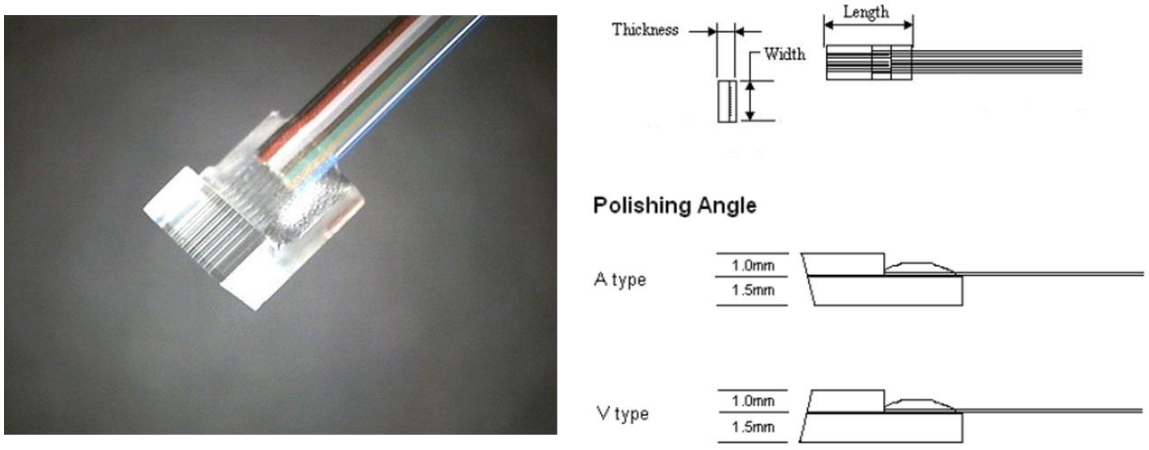

Figure 4.4 Precision Micro-Optics fiber-array diagram (Left) and with its dimension on the right.

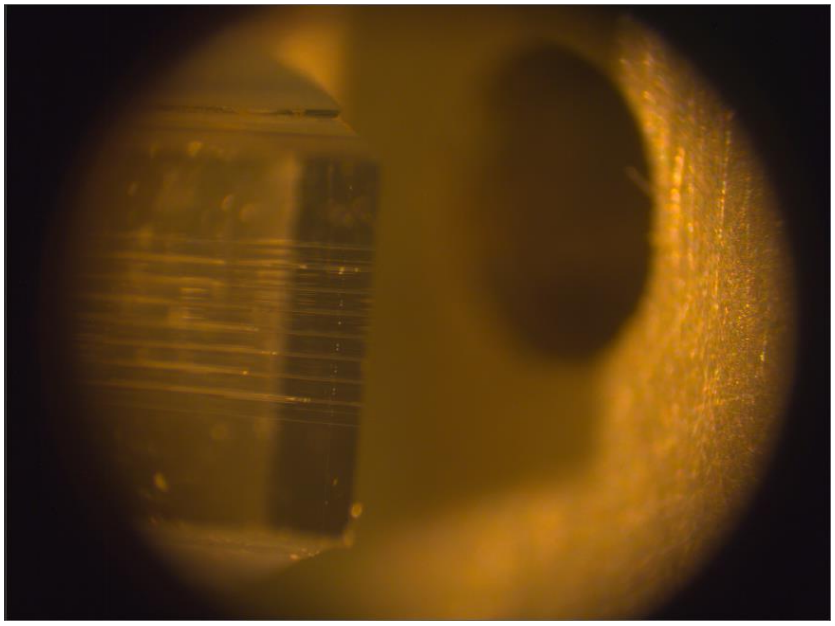

Figure 4.5 Zoom-in image of the Precision Micro-Optics fiber-array.

4.2. Detection Scheme

Figure 4.6 shows several possible detection schemes for our Si-photonic devices. The first scheme of the figure is a relatively common method and widely used in such experiments [2], [3], [9], [29]. A tunable-wavelength laser is required to be within the range of our interest. Instead of using a wavemeter one can use the wavelength information from the tunable laser. The transmitted intensity of the light at each wavelength is recorded to produce a transmission spectrum. The second scheme uses an optical spectrum analyzer (OSA) instead of a powermeter and a wavemeter. The difference between the first and second method is in the instrument. An OSA also records the transmission spectrum as a function of the wavelength.

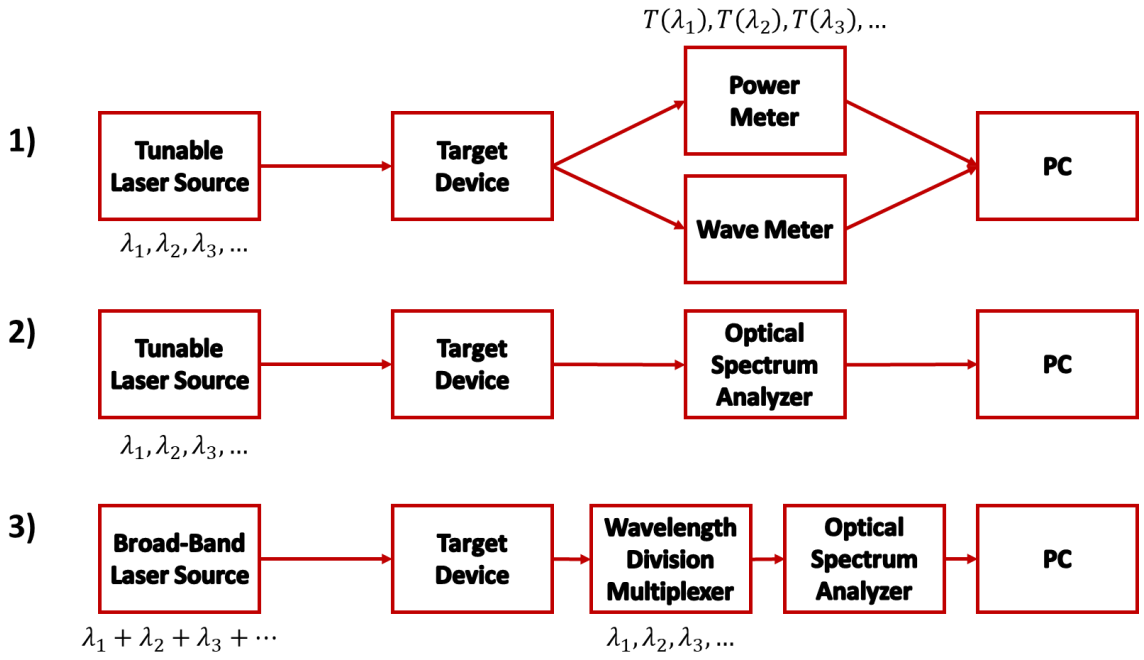

Figure 4.6 Three detection schemes for the measurement, (1) and (2) use the same input but a different measurement method. (3) A broadband source and a WDM are used.

To measure the spectrum of the ring resonator as a function of wavelength, we used a tunable laser source (OptiLab RTL-1550) and the resulting optical signal is detected by the OSA. Detailed measurement equipment is listed in Table 4.2. We measured the transmitted power of the light and plotted the data to obtain full spectrum analysis, as shown in Figure 4.7. The optical signal is recorded by the OSA as the laser wavelength is tuned at a constant rate using its sweeping function.

A broadband source (Agilent 83437A) can also be used to measure a transmission spectrum of a device and to determine Bragg wavelength of the I/O grating couplers. Instead of using a PC to analyze the data, OSA can directly provide the measured spectrum of the device. A broadband source has a wide range of working wavelengths which can be detected by the OSA. As this detection scheme gives us more flexibility, we employ this approach as the main characterization method. Table 4.2 shows the measurement equipment list for the experiment.

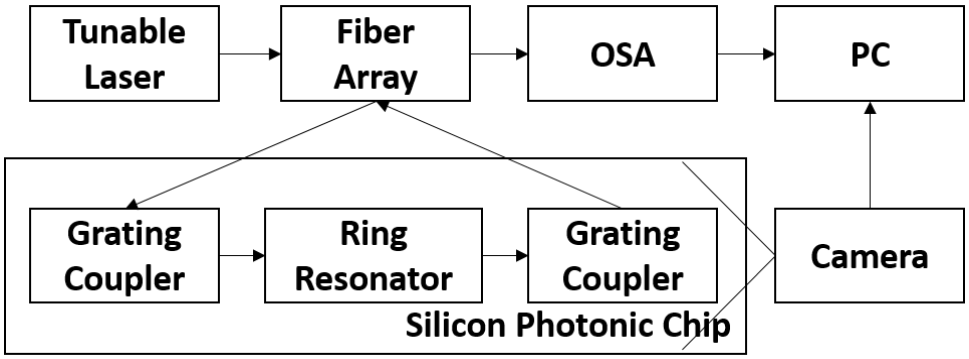

Figure 4.7 Detection scheme of the ring resonator. Sweeping the wavelengths of tunable laser source, transmission spectrum of the ring resonator device is recorded via the OSA. A microscopic lens is adopted to align the fiber array along the grating couplers.

Table 4.2 Specifications of the measurement setup.

Input Source	OptiLab RTL-1550 (Tunable Laser)	- Tuning range of 55 nm (1520 to 1575 nm) - More than 0.024 nm of resolution
Camera (Navitar) (Model Numbers are shown in Figure 4.3)	Top-View Camera	- Up to about 67X magnification - Up to about 1 um of resolve limit - Numerical Aperture of 0.28 - Relatively short working distance, 33 mm
	Bottom-View Camera	- Up to about 17X magnification - Up to about 6 um of resolve limit - Numerical Aperture of 0.053 - Relatively long working distance, 113 mm
Detector	FPM-8210 (Power Meter)	- Wavelength span from 850 nm to 1650 nm - Power range from +20 to -70 dBm - 50 millisecond of sampling rate - FC/PC, FC/APC - Data can be transferred
	Optical Spectrum Analyzer (86142B)	- Wavelength spans from 600 to 1700 nm - 0.2 nm to full range and zero span - Max sweep rate is typically 40 nm/56.3 ms - Data communication through GPIB

4.3. Measurements

4.3.1. Fabricated Silicon Devices

Some selected ring-resonator devices are presented in this section as visual verification of our design. The microscopic images and the scanning-electron microscopic (SEM) images are given for some features of the design. Due to the resolution limit of the SEM machine (Hitachi TM3000) in our institute, we cannot resolve the grating pitches in the SEM images. Mask misalignments

resulted in misaligned grating corrugations of the grating couplers which introduces additional insertion loss.

Alignment circuit which consists of two grating couplers and a waveguide are captured and presented in Figure 4.8. An additional alignment unit is shown in Figure 4.9. This unit consists of 4 independent PICs which have different propagation lengths so that one can verify propagation loss without aligning each circuit individually.

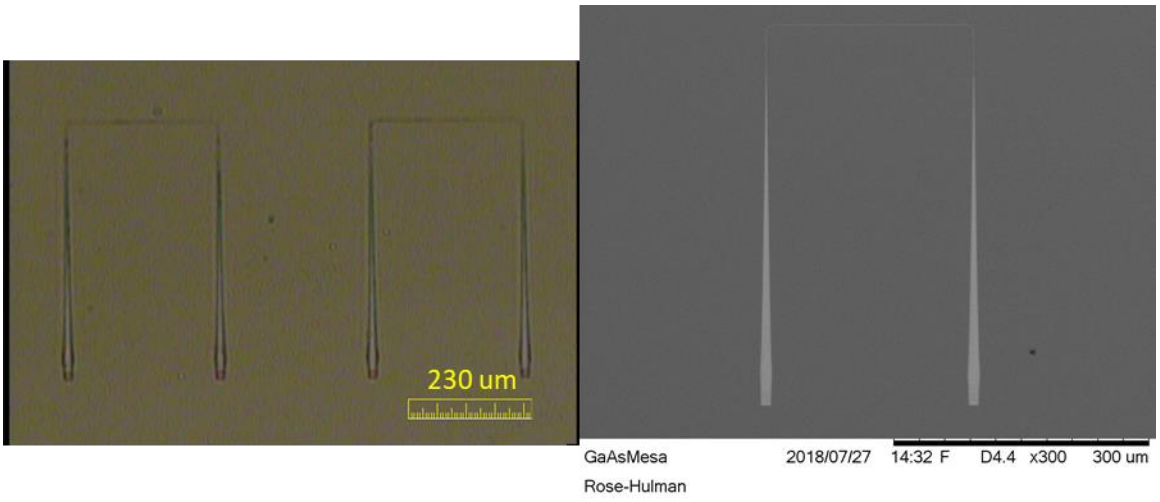

Figure 4.8 The silicon photonic device in the above figure is used to verify alignments between the grating-couplers and the fiber-array. Microscopic image (left) and SEM image (right).

Figure 4.11 shows the WDM which consists of 4 different ring resonators. The ring resonators are also designed to verify simulation results and are shown in Figure 4.10 and Figure 4.12. Spiral waveguides are also fabricated and presented in Figure 4.13.

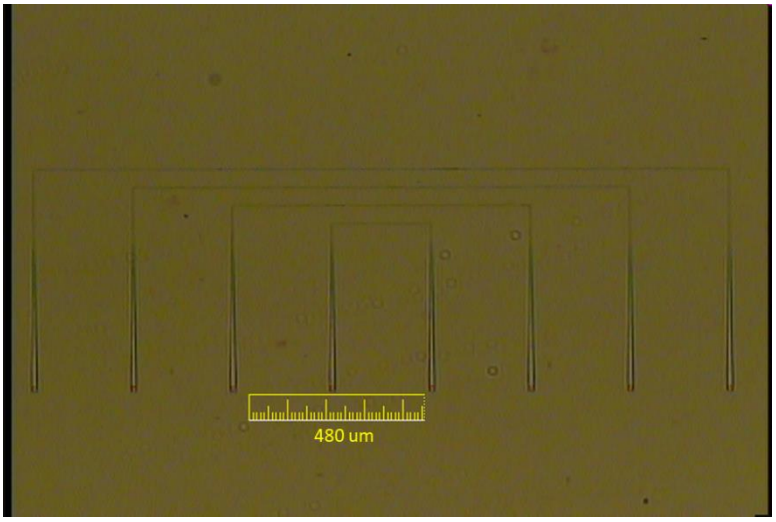

Figure 4.9 The spacing between adjacent grating couplers is 250 ± 2.63 µm. Four different circuits are designed to measure the propagation losses.

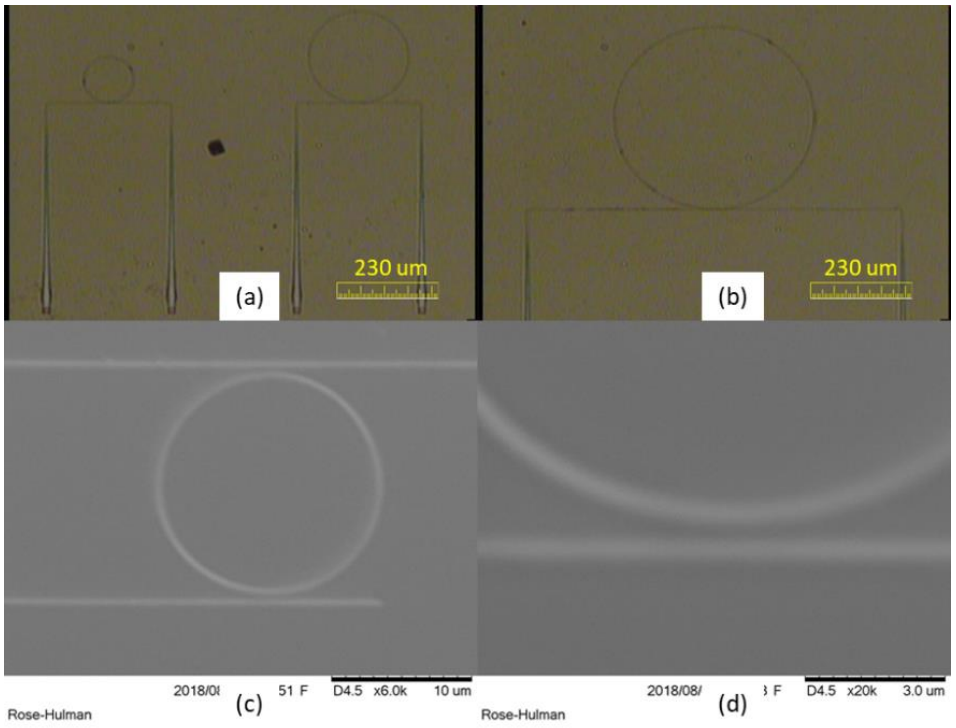

Figure 4.10 Ring-resonators (a) Device #9 and #11. (b) Device #10. (c) A ring resonator part in Device #6, and (d) its enlarged image.

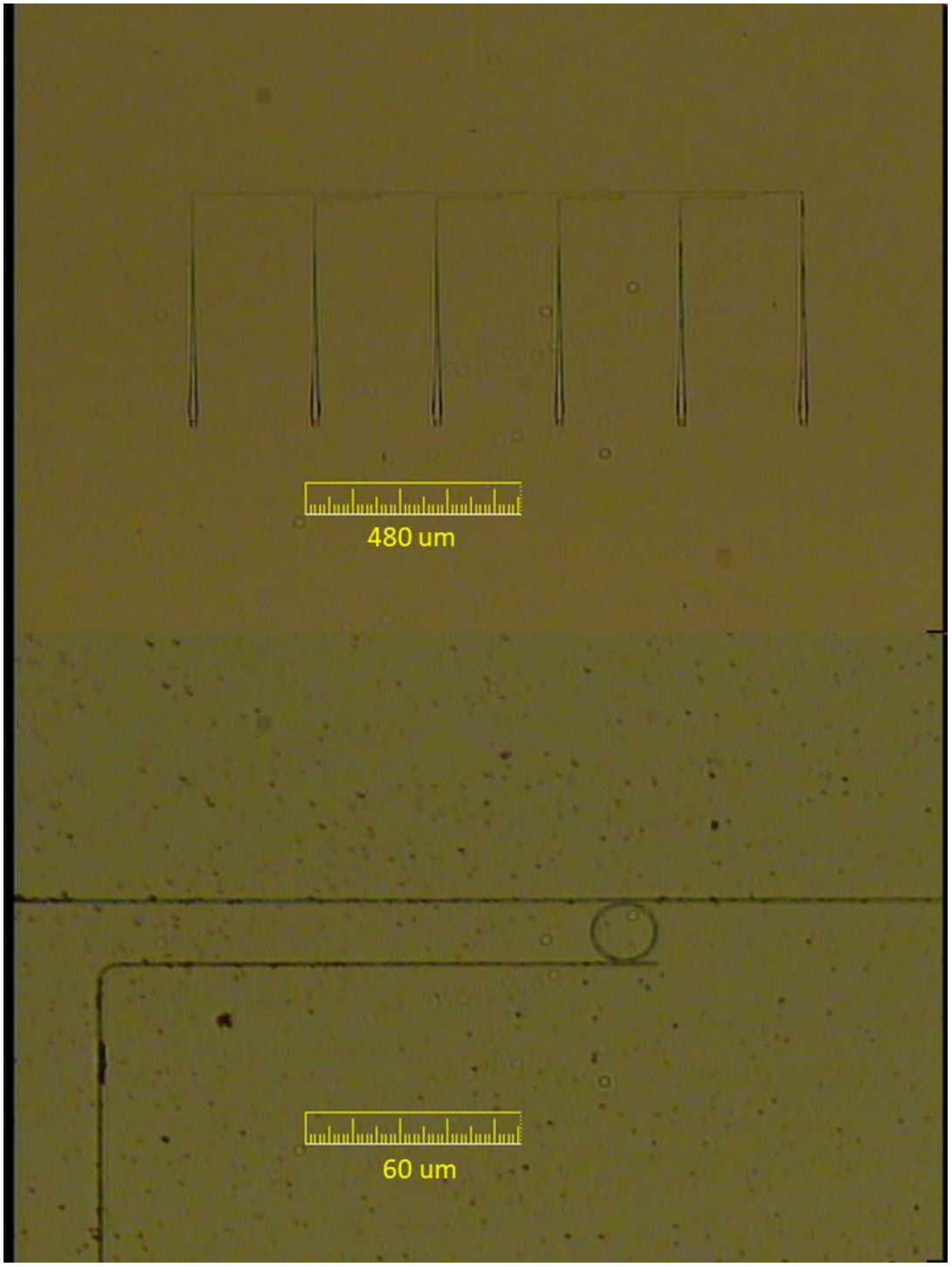

Figure 4.11 (Top) Wavelength-division multiplexer and (Bottom) enlarged image of the ring-resonator part of the WDM.

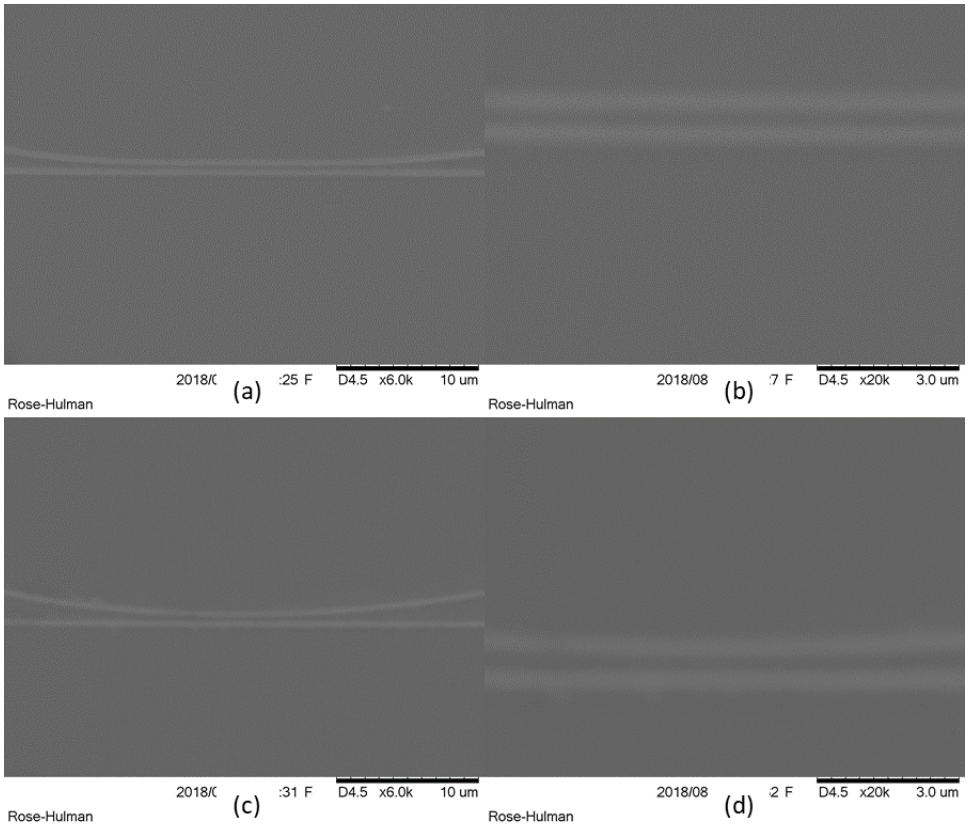

Figure 4.12 Coupling gaps between the bus waveguides and the ring-resonators. (a) A coupling region in device #14, (b) its enlarged, (c) coupling region in device #9, and (d) its enlarged image.

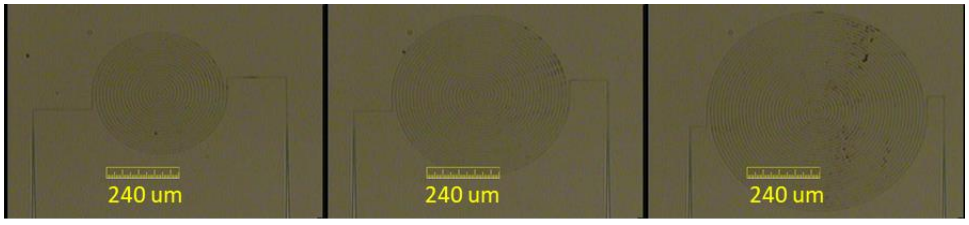

Figure 4.13 Microscope images of the spiral waveguide regions. (Left) Device #20, (Center) device #21, and (Right) device #22 are shown.

Grating couplers are fabricated by two plasma etching process. One is the full-etch and the other is the shallow-etch as we discussed in the fabrication section. After waveguides are fully

etched, shallow corrugations are etched by a designated etch depth. Since the etching processes are done in two steps, a misalignment, which will result in poor working performance of the silicon photonic device, is introduced. Figure 4.14 shows this misalignment on a set of grating couplers. Figure 4.15 also shows the same problem in the corresponding SEM images.

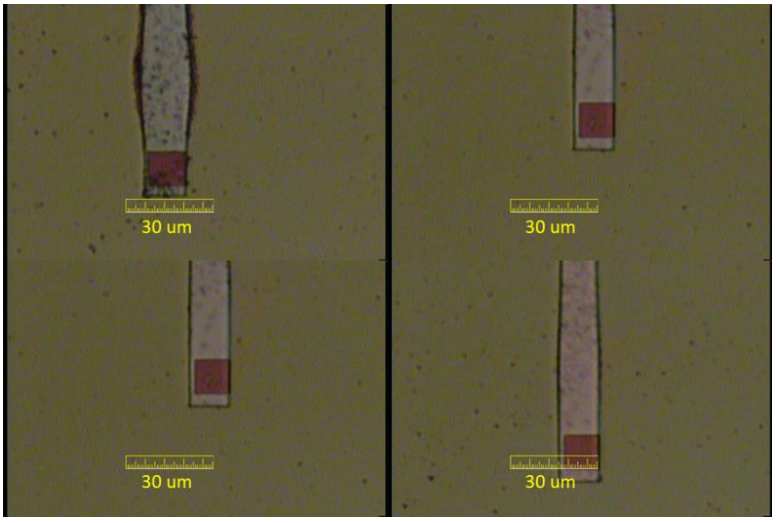

Figure 4.14 Grating pitches are misaligned to the right side of etched waveguide.

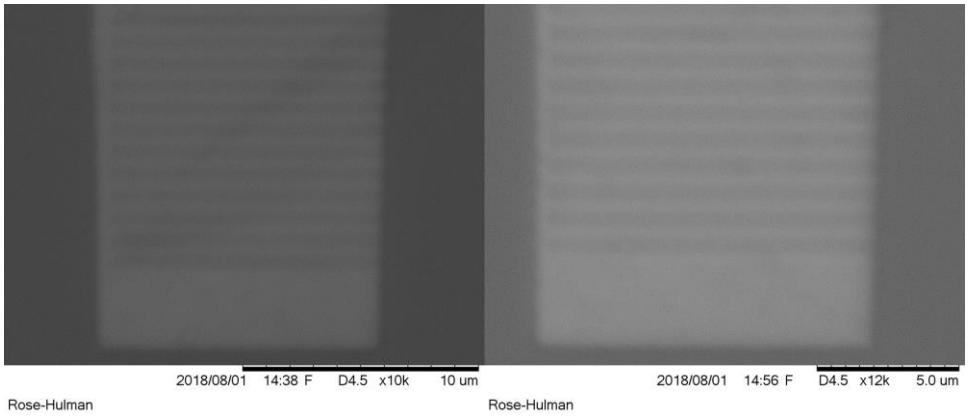

Figure 4.15 Grating corrugations are aligned on the right side of the waveguide (SEM images).

4.3.2. Alignment Sensitivity

It is very tedious and demanding to couple light into a silicon waveguide through a grating coupler because we need to be able to control and align the waveguide and the grating coupler within micrometers or even sub-micrometers accuracy. To acquire a high precision measurement performance, it is necessary to have a designated automated alignment stage. Therefore, to improve our alignment performance, we added a 3-Axis NanoMax Stage (Thorlabs, Inc.) on the existing precision stage which consisted of 10 μm resolution translation units. Because this additional stage has a fine resolution capability (less than 1μm) and offers an automated control of x-y-z translations over 20 μm using software, we were able to obtain a high-resolution control in finding an exact location of the grating couplers.

The fiber-array unit is aligned to the series of grating couplers, while the top-view camera (Thorlabs 8051-GE) and side-view camera (Cohu 4912) are monitored. A horizontal-axis is aligned first using a tilting stage and a translation stage. Then the fiber-array is translated onto the gratings. Notice that we cannot clearly see the gratings as we move the fiber-array onto the gratings (Figure 4.16 and Figure 4.17). To couple the light into the grating couplers we need to be able to adjust the fiber array and the gratings to overlap each other. We used the software from Thorlabs to scan the x and y positions of the order of microns in accuracy.

4.4. Results and Analysis

It is expected that it is not possible to acquire estimated measurements from simulations and calculations since those estimations are based on ideal conditions such as good measurement setup

and high-quality fabrication outcome. However, we were able to obtain lossy signals in terms of transmission power and wavelength information. Moreover, each ring resonator device has its own error and only a few devices worked as anticipated.

The fabrication process is the main reason for the poor performance of the devices and it consists of several characteristics such as thickness of the silicon waveguide, its width, the etch depth of the grating couplers, and the misalignment between the waveguide mask and the grating corrugation mask. It is already discussed that each error would result in a severe reduction in coupling efficiency loss [30]. According to our discussions in the fabrication section, we see the fabrication error of roughly 10%. Therefore, it is reasonable to assume those four main factors could lead to significant errors and thus making our measurement performance results to indicate a poor device performance.

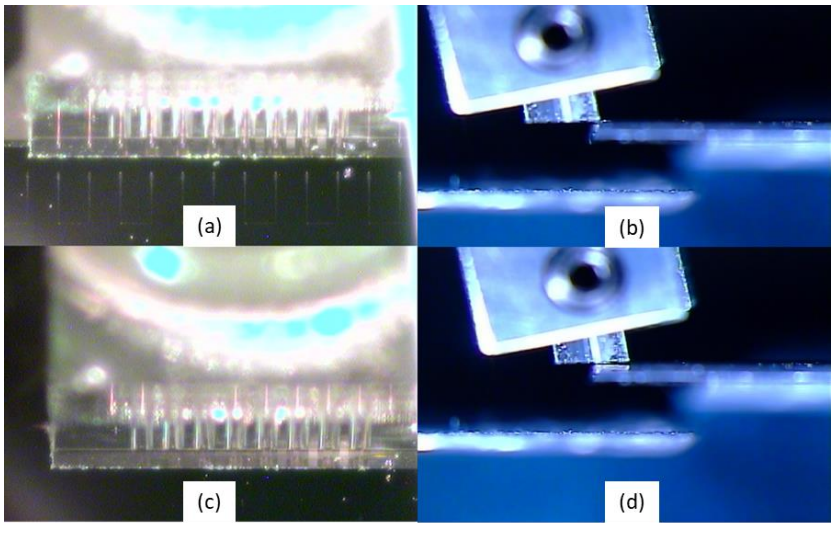

Figure 4.16 (a) Top-view and (b) side-view from the camera when the grating coupler and the fiber-array are not aligned. (c) Top-view and (d) side-view when they are aligned.

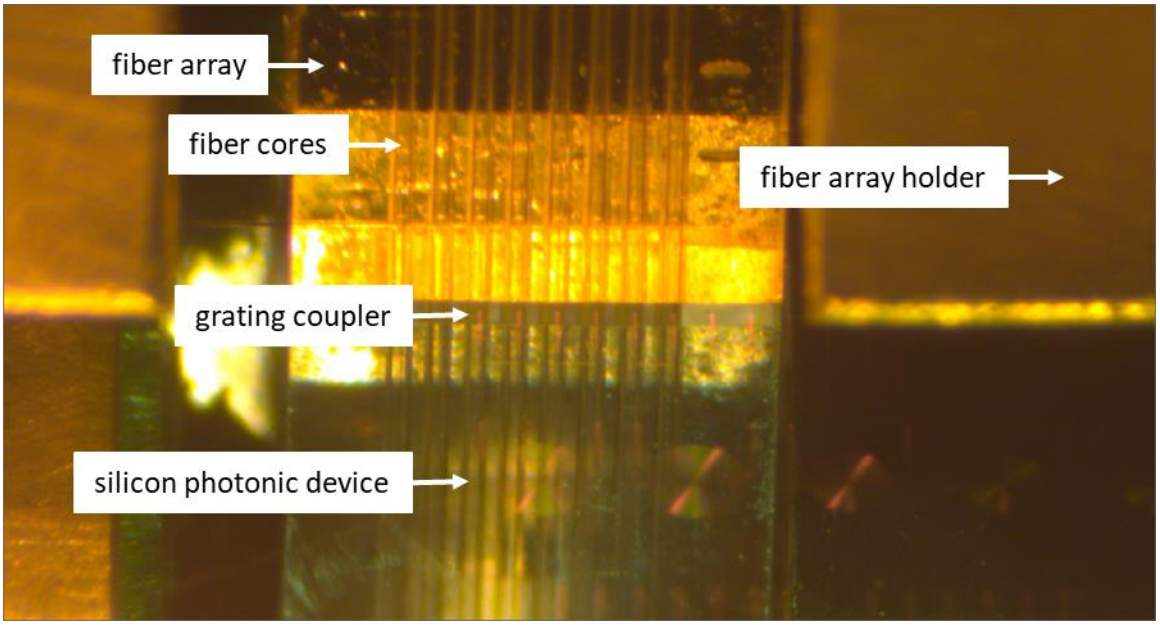

Figure 4.17 Eight fiber cores are shown and they are aligned to grating couplers.

As we discussed in the detection scheme section two kinds of input sources can be used. One is a broadband source and the other is a tunable laser source. The broadband source is used to measure a power spectrum of a ring resonator. A WDM is measured by the tunable laser source. As we can tune the wavelength of the tunable laser of the order of sub-nanometers, the tunable laser provides relatively higher resolution measurements compared to the broadband source. Moreover, we can control the wavelength tuning range so that only the desired spectrum region can be investigated.

All the devices are tested and we were only able to measure data from device #7 and device #11 (Figure 3.12 and Figure 3.17). A transmission spectrum of the ring resonator in device #11 is tested using the broadband source as an input (Figure 4.18). From the equation $\mathrm{FSR} = \lambda^2/n_g L$, assuming typical values such as $\lambda = 1550\ \mathrm{nm}$ and $n_g = 4.23$, we can calculate the FSR of 1.8

nm for the 50 μm ring resonator. Figure 4.19 shows the measured spectrum of the specified ring resonator. The measured FSR is 1.56 ± 0.1 nm which is in good agreement with the calculated value. While we observe unwanted large loss over the spectrum (over 80 dB), we are still able to define the FSR of the ring resonator.

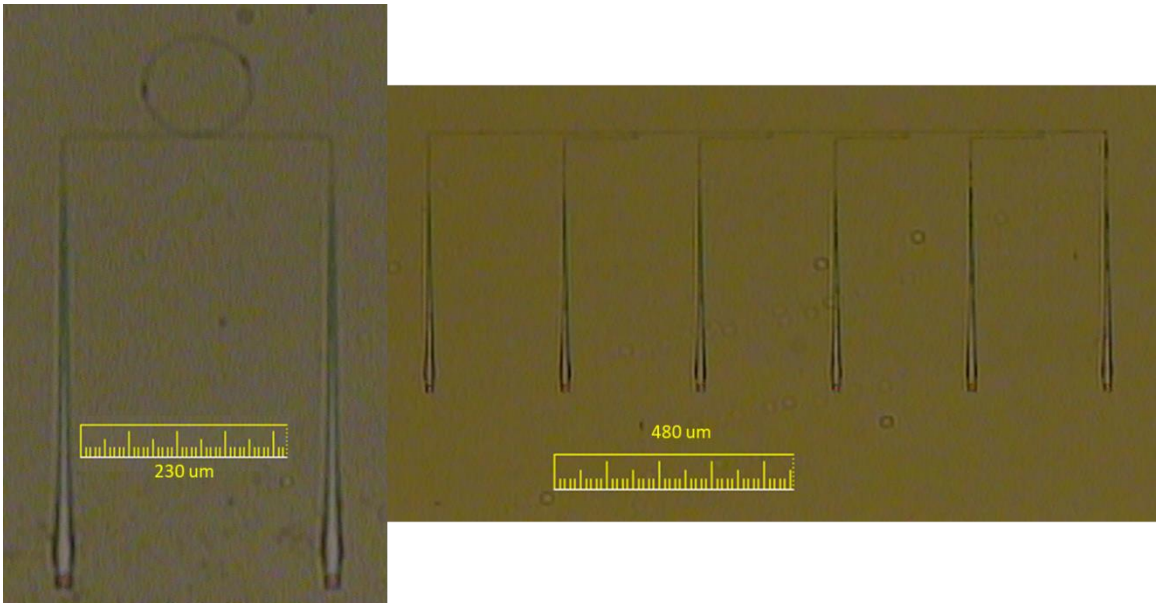

Figure 4.18 (Left) Tested ring resonator in device #11. (Right) Tested WDM circuit in device #7.

An optical power spectrum of the WDM (Device #7, Figure 4.18) is obtained and shown in Figure 4.20. Twenty consecutive measurements are averaged out by OSA before the average value is recorded by a PC. All the data is an average value of 20 measurements. So, a measurement of 0.01 dB is determined by the resolution of the OSA. The WDM consists of 4 channels and each channel passes its own specific wavelength region and filters out the rest of the wavelength range. Because of the measurement noise, a low pass filter is applied to the measured data to smoothen

the spectrum and it is shown in Figure 4.21. The first channel has the FWHM of 1.88 ± 0.01 nm at the central wavelength of 1544.9 ± 0.1 nm. Its peak optical power is -76.58 ± 0.01 dB, while its minimum power is -93.58 ± 0.01 dB. The central wavelength and FWHM of the second channel are 1547.8 ± 0.1 nm and 1.88 ± 0.01 nm, respectively. Its maximum power is -75.15 dB and minimum power is -93.58 ± 0.01 dB. The central wavelength and FWHM of the third and fourth channels are 1550.8 ± 0.1 nm and 1.8 ± 0.01 nm and 1553.4 ± 0.1 nm and 1.74 ± 0.01 nm, respectively. The maximum power of the third and fourth channels are -71.67 ± 0.01 dB and -72.88 ± 0.01 dB. The minimum power of the third and fourth channels have the same value of -93.58 ± 0.01 dB (Table 4.3).

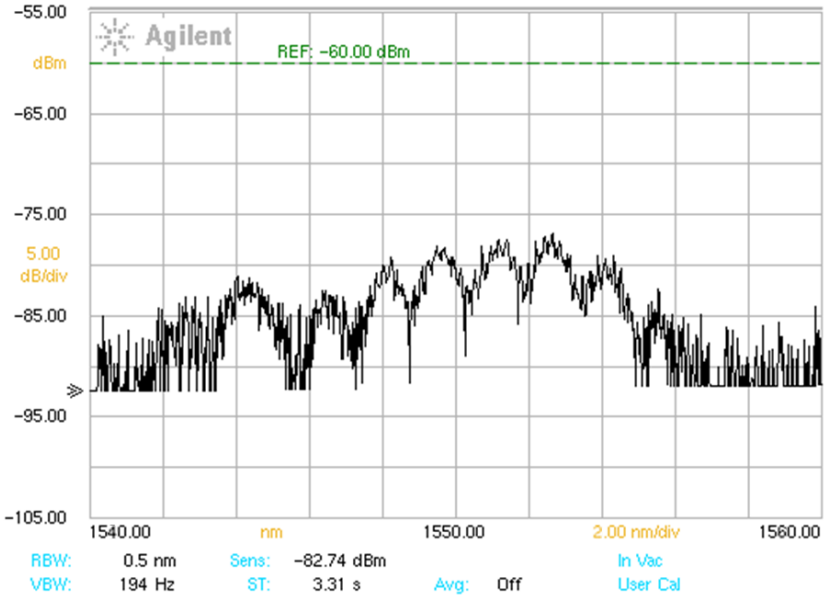

Figure 4.19 Spectrum of a ring resonator with radius of 50 µm and a directional-coupler gap of 200 nm. The measured FSR is 1.56 ± 0.1 nm.

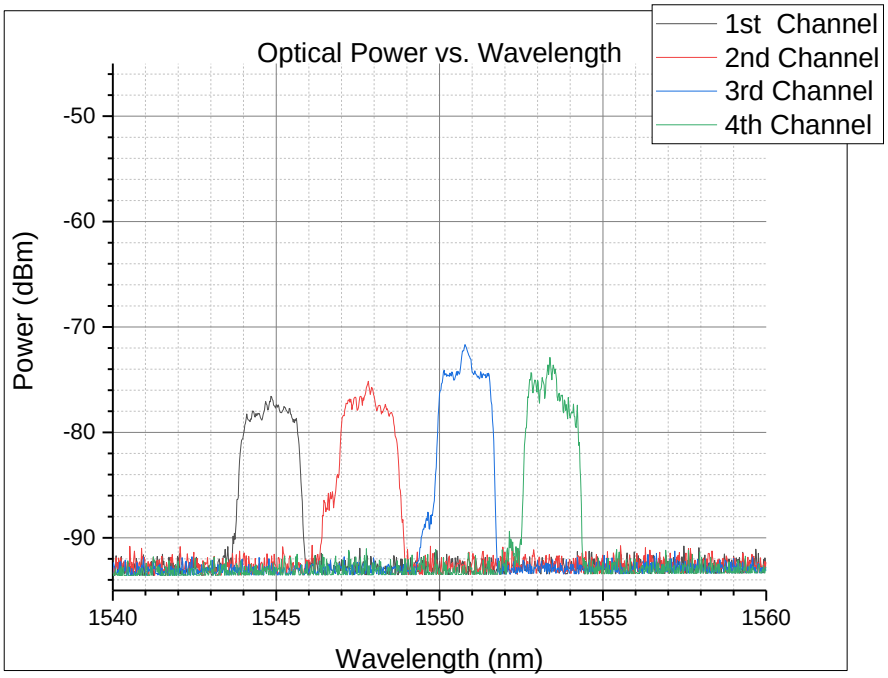

Figure 4.20 Optical power spectrum of the integrated WDM device #7 measured using the tunable laser source.

Table 4.3 Measurement data from the integrated WDM device #7.

	1st Channel	2nd Channel	3rd Channel	4th Channel
Central Wavelength (nm)	1544.9 ± 0.1	1547.8 ± 0.1	1550.8 ± 0.1	1553.4 ± 0.1
FWHM (nm)	1.88 ± 0.01	1.88 ± 0.01	1.8 ± 0.01	1.74 ± 0.01
Maximum Power (dB)	-76.58 ± 0.01	-75.15 ± 0.01	-71.67 ± 0.01	-72.88 ± 0.01
Minimum Power (dB)	-93.58 ± 0.01	-93.58 ± 0.01	-93.58 ± 0.01	-93.58 ± 0.01

4.5. Discussion on Measurement Error

To compare the measured data with the simulation results, additional inspections are required. The four main sources of the error are mentioned and discussed briefly in the previous section.

First, the thickness of the silicon layer at the grating coupler is directly related to the roughness of the wafer and its variation is shown in Figure 3.29. As the silicon layer thickness varies from 200 nm to 220 nm, the coupling efficiency drops to less than its desired efficiency (Figure 4.22).

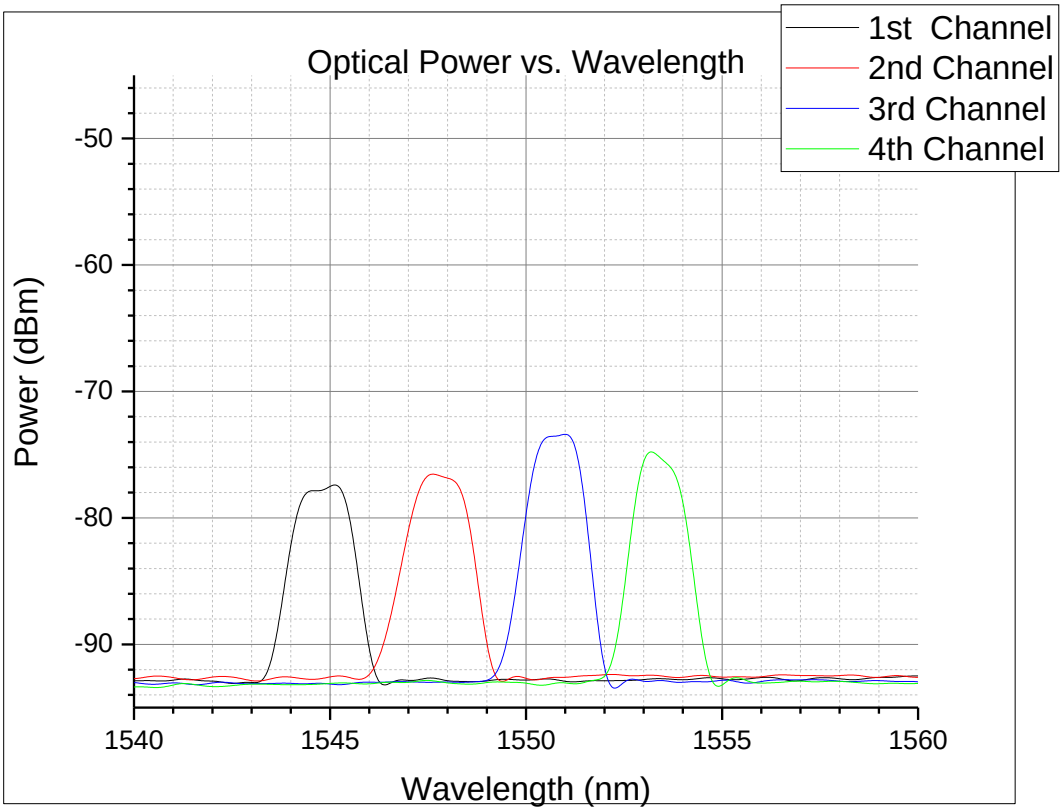

Figure 4.21 Filtered optical power spectrum of the WDM device #7.

Secondly, an etch depth of the grating corrugations is another factor of the coupling loss. The etch depth was supposed to be 70 nm, but it fluctuates between 90 nm and 120 nm (Figure 4.23) because of the over-exposure by e-beam and over-etch after the exposure. The transmittance of the

grating coupler drops from 50% to less than 10% as the etch depth varies (Figure 4.24). If the two grating couplers are considered, then the total loss increases from 6 dB to more than 20 dB.

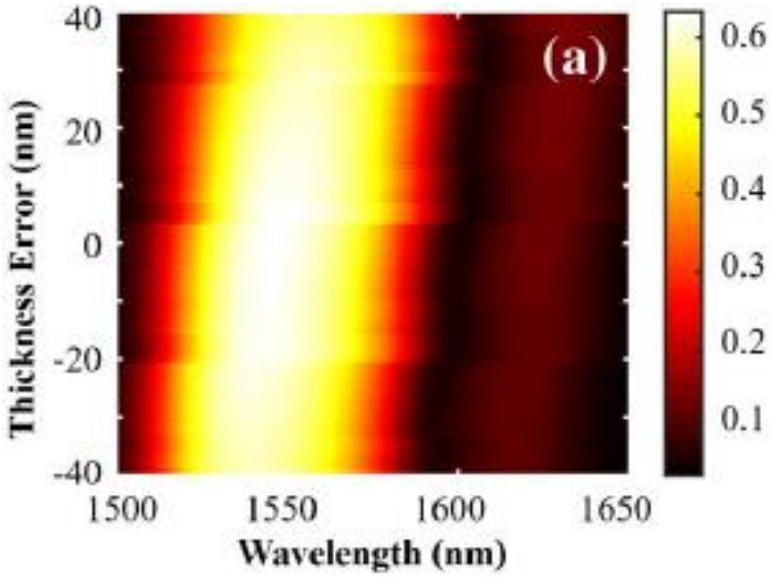

Figure 4.22 Coupling efficiency versus the fabrication error [30]**. Thickness error of the silicon waveguide. Color bar represents efficiency.**

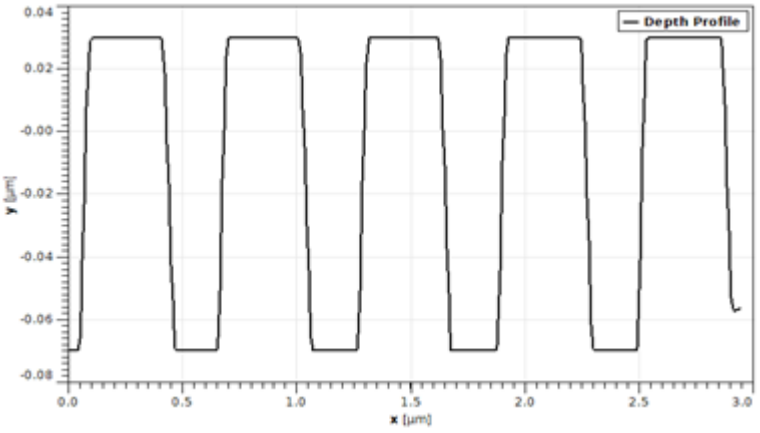

Figure 4.23 Depth profile of a grating coupler is measured by Atomic Force Microscopy. The etch depth varies from 90 nm to 120 nm while the desired depth is 70 nm.

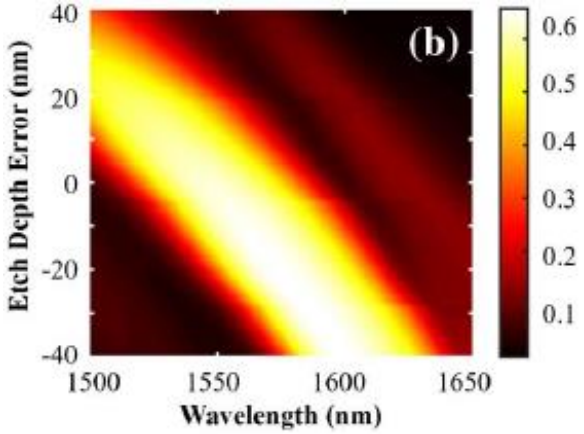

Figure 4.24 Coupling efficiency versus the fabrication error [30]**. Grating etch depth error in the etching process. Color bar represents efficiency.**

Another fabrication problem during the E-beam lithography process can be observed the SEM imaging of the devices. Since the grating coupler needs two etch steps and two different masks they should be precisely aligned. However, the misalignment between the first etch and the second etch is detected and shown in Figure 4.25. The grating lines of the grating coupler are not properly etched out at the edge of the coupler. The transmittance of the grating coupler drops from 50% to less than 40% as this misalignment occurs (Figure 4.26).

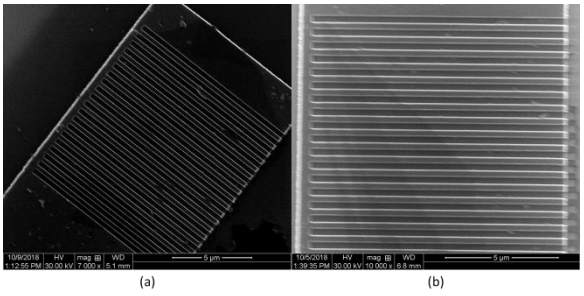

Figure 4.25 SEM image of (a) the misalignment due to the second exposure and (b) its enlarged version.

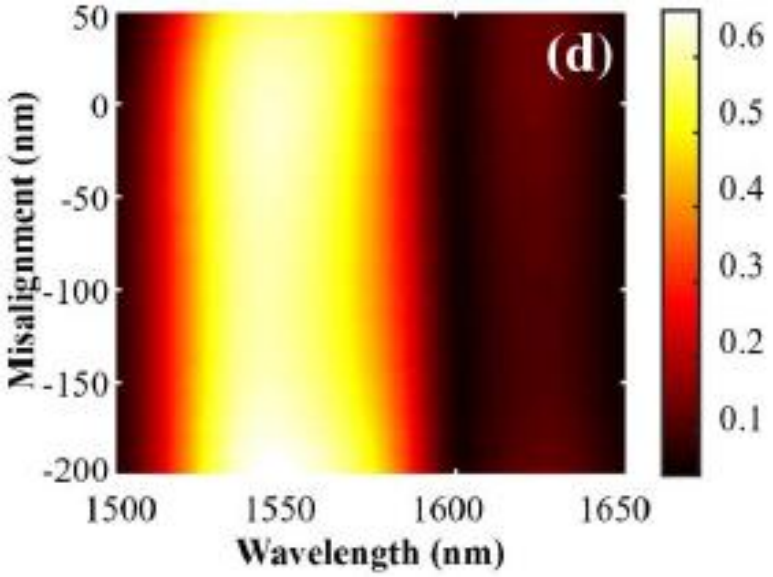

Figure 4.26 Coupling efficiency versus fabrication error [30]**. Misalignment between the two e-beam lithography steps. Color bar represents the efficiency.**

5. CONCLUSIONS

The primary goal of this thesis is to build ring-resonator based silicon photonic sensor devices and an experimental apparatus for evaluating the device performance. First, the ring resonators are modeled and characteristics of the WDM devices are discussed, then are performed. Modeling and simulations of the ring-resonator circuits and the WDM devices are presented and analyzed. Grating couplers are designed and simulated as I/O devices of the ring-resonators. The device fabrication was done in collaboration with the University of Minnesota because a high-precision fabrication facility is required to build such nanometer scale silicon photonic devices.

Various geometrical parameters such as the radius of a ring, the coupling length, and the gap between a ring and a bus waveguide are explored and analyzed in terms of related device parameters such as its center wavelength of operation, wavelength shift, and FSR. We demonstrated the ring resonator and the WDM device and presented the measured data. The optical spectrum of the ring resonator shows the FSR of 1.56 ± 0.1 nm which is in good agreement with the simulated FSR, 1.8 nm. An average of measured channel spacing between four channels is 1.825 ± 0.1 nm which is in good agreement with the simulation result of 2 nm for the WDM device. However, the measured spectra show some discrepancies in terms of optical power transmission due to the imperfections in the fabrication process and experimental setups.

Fabrication is considered as the main contributor to the optical power leakage or loss as we discussed in the results section 4.4. As we were not able to verify all structures of the fabricated devices visually without the use of a high-resolution SEM machine, we could only rely on images on some portion of features provided by the University of Minnesota. It is reasonable to assume

that the thickness errors are present all over the wafer just as much as on the measured devices. Fabrication errors such as waveguide geometrics, the roughness of the silicon layer on the wafer, and the precise mask alignments are highly required to be resolved in order to build a high-performance silicon photonic device.

To measure fabricated devices successfully a high-precision experimental setup is required. Since the alignment must be controlled in the order of sub-microns and manual alignment requires numerous trials and it is never going to be stable and consistent. Automated experimental setup is highly recommended for silicon photonic devices to measure the data with consistency and reliability.

LIST OF REFERENCES

[1] C. J. Smith, R. Shankar, M. Laderer, M. B. Frish, M. Loncar, and M. G. Allen, "Sensing nitrous oxide with QCL-coupled silicon-on-sapphire ring resonators," *Opt. Express*, vol. 23, no. 5, pp. 5491–5499, 2015.

[2] J. T. Robinson, L. Chen, and M. Lipson, "On-chip gas detection in silicon optical microcavities," *Opt. Express*, vol. 16, no. 6, pp. 4296–4301, 2008.

[3] D.-X. Xu *et al.*, "Label-free biosensor array based on silicon-on-insulator ring resonators addressed using a WDM approach," *Opt. Lett.*, vol. 35, no. 16, pp. 2771–2773, 2010.

[4] W. Bogaerts *et al.*, "Silicon microring resonators," *Laser Photon. Rev.*, vol. 6, no. 1, pp. 47–73, 2012.

[5] T. H. Stievater *et al.*, "Trace gas absorption spectroscopy using functionalized microring resonators," *Opt. Lett.*, vol. 39, no. 4, pp. 969–972, 2014.

[6] A. Nitkowski, L. Chen, and M. Lipson, "Cavity-enhanced on-chip absorption spectroscopy using microring resonators," *Opt. Express*, vol. 16, no. 16, pp. 11930–11936, 2008.

[7] A. Nitkowski, A. Baeumner, and M. Lipson, "On-chip spectrophotometry for bioanalysis using microring resonators," *Biomed. Opt. Express*, vol. 2, no. 2, pp. 271–277, 2011.

[8] E. Ryckeboer, R. Bockstaele, M. Vanslembrouck, and R. Baets, "Glucose sensing by waveguide-based absorption spectroscopy on a silicon chip," *Biomed. Opt. Express*, vol. 5, no. 5, pp. 1636–1648, 2014.

[9] D.-X. Xu *et al.*, "Folded cavity SOI microring sensors for high sensitivity and real time measurement of biomolecular binding," *Opt. Express*, vol. 16, no. 19, pp. 15137–15148, 2008.

[10] J. Hu *et al.*, "Fabrication and testing of planar chalcogenide waveguide integrated microfluidic sensor," *Opt. Express*, vol. 15, no. 5, pp. 2307–2314, 2007.

[11] A. Yariv, "Universal relations for coupling of optical power between microresonators and dielectric waveguides," *Electron. Lett.*, vol. 36, no. 4, pp. 321–322, 2000.

[12] A. Yariv, "Critical coupling and its control in optical waveguide-ring resonator systems," *IEEE Photonics Technol. Lett.*, vol. 14, no. 4, pp. 483–485, 2002.

[13] D. G. Rabus, "Ring resonators: Theory and modeling," *Integr. Ring Reson. Compend.*, pp. 3–40, 2007.

[14] M. Hammer, K. R. Hiremath, and R. Stoffer, "Analytical approaches to the description of optical microresonator devices," in *AIP conference proceedings*, 2004, vol. 709, no. 1, pp.

48–71.

[15] X. Zheng *et al.*, “A tunable 1x4 silicon CMOS photonic wavelength multiplexer/demultiplexer for dense optical interconnects,” *Opt. Express*, vol. 18, no. 5, pp. 5151–5160, 2010.

[16] P. Dong *et al.*, “Low power and compact reconfigurable multiplexing devices based on silicon microring resonators,” *Opt. Express*, vol. 18, no. 10, pp. 9852–9858, 2010.

[17] J. E. Cunningham *et al.*, “Highly-efficient thermally-tuned resonant optical filters,” *Opt. Express*, vol. 18, no. 18, pp. 19055–19063, 2010.

[18] S. Xiao, M. H. Khan, H. Shen, and M. Qi, “Multiple-channel silicon micro-resonator based filters for WDM applications,” *Opt. Express*, vol. 15, no. 12, pp. 7489–7498, 2007.

[19] W. R. McKinnon *et al.*, “Extracting coupling and loss coefficients from a ring resonator,” *Opt. Express*, vol. 17, no. 21, pp. 18971–18982, 2009.

[20] F. Xia, L. Sekaric, and Y. A. Vlasov, “Mode conversion losses in silicon-on-insulator photonic wire based racetrack resonators,” *Opt. Express*, vol. 14, no. 9, pp. 3872–3886, 2006.

[21] S. J. McNab, N. Moll, and Y. A. Vlasov, “Ultra-low loss photonic integrated circuit with membrane-type photonic crystal waveguides,” *Opt. Express*, vol. 11, no. 22, pp. 2927–2939, 2003.

[22] F. Van Laere *et al.*, “Compact focusing grating couplers for silicon-on-insulator integrated circuits,” *IEEE Photonics Technol. Lett.*, vol. 19, no. 23, pp. 1919–1921, 2007.

[23] Y. Wang, J. Flueckiger, C. Lin, and L. Chrostowski, “Universal grating coupler design,” in *Photonics North 2013*, 2013, vol. 8915, p. 89150Y.

[24] D. Taillaert *et al.*, “Grating couplers for coupling between optical fibers and nanophotonic waveguides,” *Jpn. J. Appl. Phys.*, vol. 45, no. 8R, p. 6071, 2006.

[25] Y. Wang *et al.*, “Fully etched grating coupler with low back reflection,” in *Photonics North 2013*, 2013, vol. 8915, p. 89150U.

[26] Y. Wang *et al.*, “Focusing sub-wavelength grating couplers with low back reflections for rapid prototyping of silicon photonic circuits,” *Opt. Express*, vol. 22, no. 17, pp. 20652–20662, 2014.

[27] Z. Yu *et al.*, “High efficiency and broad bandwidth grating coupler between nanophotonic waveguide and fibre,” *Chinese Phys. B*, vol. 19, no. 1, p. 5, 2010.

[28] J. C. Wirth, “Silicon grating couplers for low loss coupling between optical fiber and silicon nanowires,” *Purdue Univ.*, 2011.

[29] C. J. Smith, R. Shankar, M. Laderer, M. B. Frish, M. Loncar, and M. G. Allen, “Sensing nitrous oxide with QCL-coupled silicon-on-sapphire ring resonators,” *Opt. Express*, vol. 23, no. 5, p. 5491, 2015.

[30] Y. Tong, W. Zhou, and H. K. Tsang, “Efficient perfectly vertical grating coupler for multi-core fibers fabricated with 193 nm DUV lithography,” *Opt. Lett.*, vol. 43, no. 23, pp. 5709–5712, 2018.

APPENDICES

APPENDIX A – Fiber Array Holder CAD Design

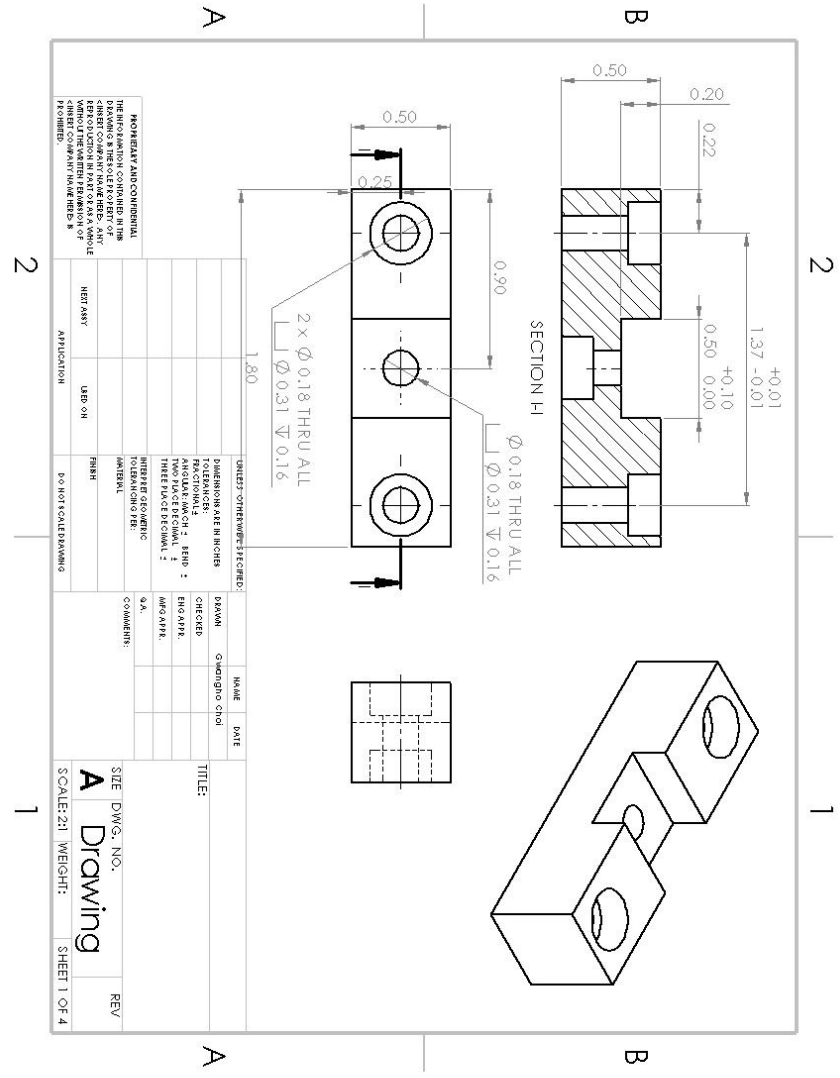

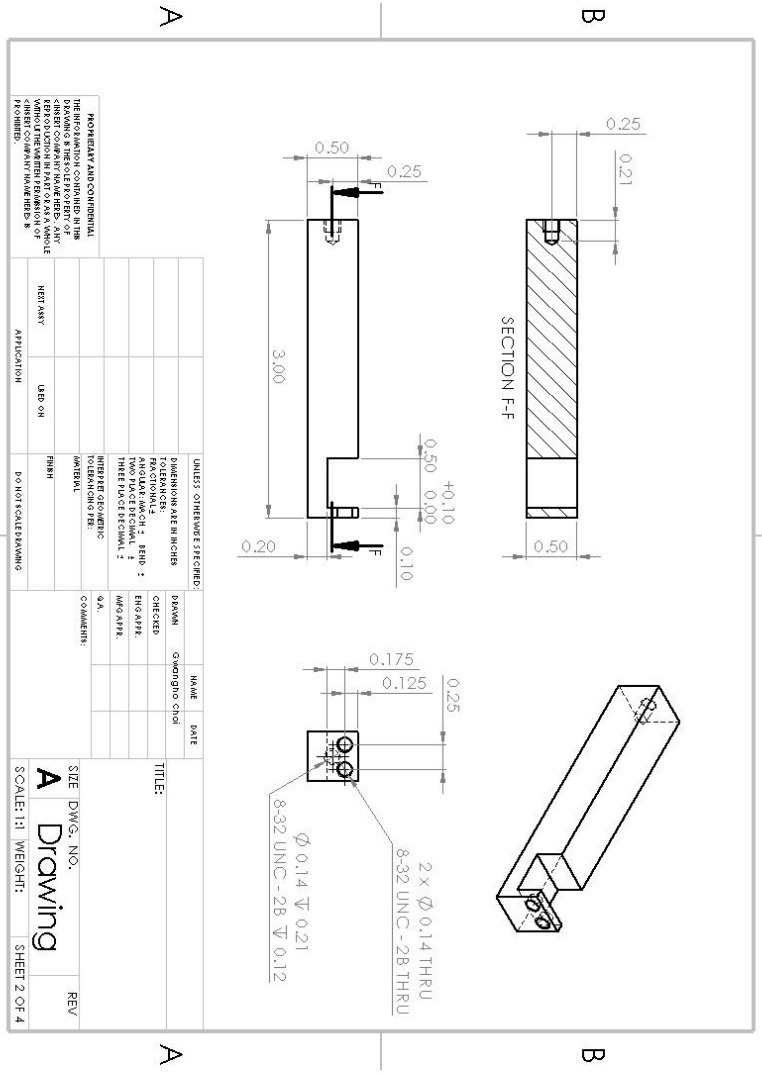
SECTION F-F
0.25
0.21
0.50
0.50
0.25
3.00
0.20
0.10
+0.10
0.00
0.50
0.175
0.125
0.25
2 × Ø 0.14 THRU
8-32 UNC - 2B THRU
Ø 0.14 ↧ 0.21
8-32 UNC - 2B ↧ 0.12
PROPRIETARY AND CONFIDENTIAL
THE INFORMATION CONTAINED IN THIS DRAWING IS THE SOLE PROPERTY OF <INSERT COMPANY NAME HERE>. ANY REPRODUCTION IN PART OR AS A WHOLE WITHOUT THE WRITTEN PERMISSION OF <INSERT COMPANY NAME HERE> IS PROHIBITED.
NEXT ASSY
USED ON
APPLICATION
DO NOT SCALE DRAWING
UNLESS OTHERWISE SPECIFIED:
DIMENSIONS ARE IN INCHES
TOLERANCES:
FRACTIONAL ±
ANGULAR: MACH ± BEND ±
TWO PLACE DECIMAL ±
THREE PLACE DECIMAL ±
INTERPRET GEOMETRIC TOLERANCING PER:
MATERIAL
FINISH
NAME
DATE
DRAWN
Gwangno Choi
CHECKED
ENG APPR.
MFG APPR.
Q.A.
COMMENTS:
TITLE:
SIZE
A
DWG. NO.
Drawing
REV
SCALE: 1:1
WEIGHT:
SHEET 2 OF 4

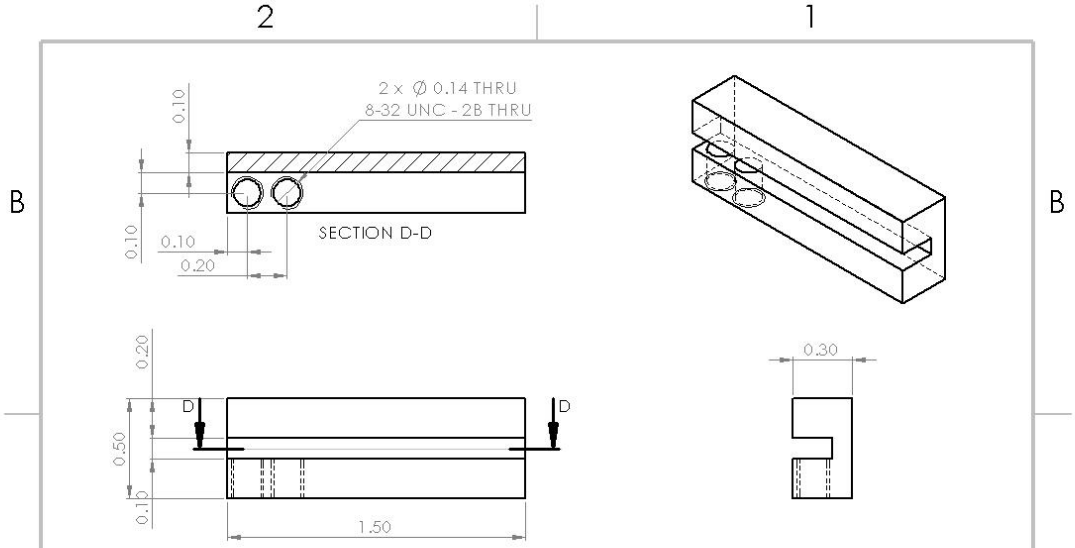

		UNLESS OTHERWISE SPECIFIED:		NAME	DATE
		DIMENSIONS ARE IN INCHES TOLERANCES: FRACTIONAL ± ANGULAR: MACH ± BEND ± TWO PLACE DECIMAL ± THREE PLACE DECIMAL ±	DRAWN	Gwangho Choi	
			CHECKED		
			ENG APPR.		
			MFG APPR.		
		INTERPRET GEOMETRIC TOLERANCING PER:	Q.A.		
		MATERIAL	COMMENTS:		
NEXT ASSY	USED ON	FINISH			
APPLICATION		DO NOT SCALE DRAWING			

TITLE:

SIZE	DWG. NO.	REV
A	Drawing	
SCALE: 2:1	WEIGHT:	SHEET 3 OF 4

APPENDIX B – Simulation Code for Wavelength Division Multiplexer

ring_resonator.lsf

```
########################################################
# file: ring_resonator.lsf
#
# Description: Send transmission through ring resonator to
# Visualizer. Transmission data comes from 3
# different sources: an .ldf with 3D FDTD data,
# a MODE Solutions propagator simulation and an
# analytical formula
#
#
# Copyright 2012, Lumerical Solutions, Inc.
########################################################

# FDTD results
loaddata("fdtd_results.ldf");

########################################################
# Results from Propagator
# ring resonator design parameters
lambda0 = 1.55e-6; # center wavelength
FSR = 3200e9*lambda0^2/c; # free spectral range in m
Q = 2000; # Q

# get data from propagator simulation;
T = getresult("drop",'T');
Tdrop_propagator = -T.T;
lambda = c/T.f;
########################################################

########################################################
# Calculation of theory
tau_11 = sqrt((lambda*pi/FSR/Q/2)^2+1)-(lambda*pi/FSR/Q/2);
tau_12 = sqrt(1-abs(tau_11)^2);

# offset the phase for a particular peak wavelength
peak_lambda = 1550e-9;
phase_offset = -2i*pi*peak_lambda/FSR;

Tdrop_theory = abs(tau_12)^4/abs(1-tau_11^2*exp(1i*2*pi*lambda/FSR+phase_offset))^2;
########################################################

# create dataset
T_result = matrixdataset("T_result");
T_result.addparameter("lambda",lambda);
```

```
T_result.addattribute("Tdrop_theory",Tdrop_theory);
T_result.addattribute("Tdrop_propagator",Tdrop_propagator);
T_result.addattribute("Tdrop_3DFDTD",Tdrop_3DFDTD);

visualize(T_result);
```

ring_resonator_fdtd.lsf

```
########################################################
# file: ring_resonator_fdtd.lsf
#
# Description: This file calculates the results of
# ring_resonator.fsp and saves them to
# ldf file. The final resulats are plotted
# using ring_resonator.lsf
#
# Copyright 2016, Lumerical Solutions, Inc.
########################################################

# collect data from port 2
Tdrop_dataset = getresult("FDTD::ports::port 2","T");
Tdrop_3DFDTD = abs(Tdrop_dataset.T);
lambda_3DFDTD = Tdrop_dataset.lambda;

# save data to ldf file
savedata("fdtd_results.ldf",Tdrop_3DFDTD,lambda_3DFDTD);
```

setup.lsf

```
select("ring resonator");
r = get("radius");
g = get("gap");
w = get("base width");

x_port = (r+g+w)+g;
y_port = r+g+w;
y_span = 3e-6;

# FDTD
select("FDTD");
set("x span", 3*r);set("y span", 3*r);

# Profile
select("full_profile");
set("x span", 3*r);set("y span", 3*r);

# Input
select("FDTD::ports::port 1");
```

```
set("x", -x_port);set("y", y_port);
set("y span", y_span);
set("direction", "Forward");
set("mode selection", Mode);
select("t_in");
set("x", -x_port);set("y", y_port);

# Drop
select("FDTD::ports::port 2");
set("x", -x_port);set("y", -y_port);
set("y span", y_span);
set("direction", "Forward");
set("mode selection", Mode);
select("t_drop");
set("x", -x_port);set("y", -y_port);

# Through
select("FDTD::ports::port 3");
set("x", x_port);set("y", y_port);
set("y span", y_span);
set("direction", "Backward");
set("mode selection", Mode);
select("t_through");
set("x", x_port);set("y", y_port);

# Add
select("FDTD::ports::port 4");
set("x", x_port);set("y", -y_port);
set("y span", y_span);
set("direction", "Backward");
set("mode selection", Mode);
select("t_add");
set("x", x_port);set("y", -y_port);
```

3D_ring.lsf

```
Mode = "fundamental TM mode";

radi = 8e-6;
inc_radi = 0.035e-6;
g=0.3e-6;

for (i=2:4)
{
switchtolayout;
r = radi + (i-1)*inc_radi;
select("ring resonator");
set("radius", r);
set("gap", g);
```

```
setup;
newfilename = "r"+num2str(r*1e6)+"_g"+num2str(g*1e6)+"_"+Mode;
select("::model");
set("filename", newfilename);
run;
runanalysis;
}
```